1 *Ezh2 Delays Activation of Differentiation Genes During Normal*
2 *Cerebellar Granule Neuron Development and in Medulloblastoma*

3
4

5 **Authors:** James Purzner[1,2,3*], Alexander S. Brown[3,4], Teresa Purzner[1,2,3], Lauren Ellis[3,5], Sara
6 Broski[3,6], Ulrike Litzenburger[3,7], Kaytlin Andrews[8], Aryaman Sharma[8], Xin Wang[9,10], Michael D.
7 Taylor[11], Yoon-Jae Cho[12,13,14], Margaret T. Fuller[3,15], and Matthew P. Scott[3*]

8
9

10 **Affiliations:**
11 [1]Division of Neurosurgery, Department of Surgery, Queen's University, Kingston, ON
12 [2]Department of Biomedical and Molecular Sciences, Queen's University, Kingston, ON
13 [3]Department of Developmental Biology, Stanford University School of Medicine, Stanford, CA
14 [4]EditCo Bio, Redwood City, CA
15 [5]Department of Anesthesiology, University of California Los Angeles, Los Angeles, CA.
16 [6]Nura Bio, South San Francisco, CA
17 [7]Therapeutic Oncology Research Lab Head, Nuvisan Pharma, Berlin, Germany
18 [8]Department of Medcine, Queen's University, Kingston, ON
19 [9]Clinician-Scientist Training Program, Temerty Faculty of Medicine, University of Toronto,
20 Toronto, ON
21 [10]Department of Medical Oncology, Princess Margaret Cancer Centre, Toronto, ON
22 [11]Pediatric Brain Tumor Research Program**,** Texas Children's Hospital, Houston, TX
23 [12]Division of Pediatric Neurology, Department of Pediatrics, Oregon Health & Science
24 University, Portland, Oregon USA
25 [13]Papé Family Pediatric Research Institute, Oregon Health & Science University, Portland,
26 Oregon USA
27 [14]Knight Cancer Institute, Oregon Health & Science University, Portland, Oregon USA
28 [15]Department of Genetics, Stanford University School of Medicine, Stanford, CA
29
30
31
32 *Correspondence to: mscott@stanford.edu, jgp12@queensu.ca
33
34

35 **Key Words:**
36 **cerebellum, cerebellar granule neuron, Ezh2, polycomb, PRC2, chromatin**
37 **immunoprecipitation, transcription, brain development, differentiation, medulloblastoma**

Abstract

Medulloblastoma (MB) is the most common malignant brain tumour in children. The Sonic Hedgehog (SHH)-medulloblastoma subtype arises from the cerebellar granule neuron lineage. Terminally differentiated neurons are incapable of undergoing further cell division, so an effective treatment for this tumour could be to force neuronal differentiation. Differentiation therapy provides a potential alternative for patients with medulloblastoma who harbor mutations that impair cell death pathways (TP53), which is associated a with high mortality. To this end, our goal was to explore epigenetic regulation of cerebellar granule neuron differentiation in medulloblastoma cells. Key regulators were discovered using chromatin immunoprecipitation with high-throughput sequencing. DNA-bound protein and chromatin protein modifications were investigated across all genes. We discovered that Ezh2-mediated tri-methylation of the H3 histone (H3K27me3), occurred on more than half of the 787 genes whose transcription normally increases as granule neurons terminally differentiate. Conditional knockout of *Ezh2* led to early initiation of differentiation in granule neuron precursors (GNPs), but only after cell cycle exit had occurred. Similarly, in MB cells, neuronal differentiation could be induced by preventing H3K27me3 modifications using an Ezh2 inhibitor (UNC1999), but only when UNC1999 was combined with forced cell cycle exit driven by a CDK4/6 inhibitor (Palbociclib). Ezh2 emerges as a powerful restraint upon post-mitotic differentiation during normal GNP development and combination of Ezh2 inhibition with cell cycle exit leads to MB cell differentiation.

Introduction

59

60   The Hedgehog (Hh) pathway is one of the major regulators of cerebellar granule neuron

61   precursor (GNP) proliferation. Sonic hedgehog (Shh) protein secreted from Purkinje neurons

62   drives proliferation of GNPs (*1-3*) through transcriptional regulation of *Cyclin D1* and *N-myc* (*4,*

63   *5*) among other targets. Despite ongoing exposure to Shh, GNPs leave the cell cycle and

64   undergo timed and reliable differentiation, a switch that occurs correctly about 50 billion times

65   in the developing human brain. When differentiation and neurogenesis fail, for example due to

66   Shh pathway mutations that lead to unrestrained Shh target gene activation, GNPs continue to

67   proliferate and may form medulloblastomas (MBs). Yet even in genetic models of MB that are

68   100% penetrant, where Shh target genes are dramatically activated, the vast majority of GNPs

69   still differentiate into functional granule neurons (GNs) (*6*). Thus, regulation that promotes

70   differentiation has the potential to overcome a potent mitogenic signal.

71   GNPs are the cell type of origin for the Shh subtype of MBs, which make up a quarter to a

72   third of MBs. Children with Shh MB are treated intensively with surgical resection followed by

73   craniospinal radiation, one year of multi-drug chemotherapy, and targeted inhibition of the Hh

74   pathway using Smo inhibitors. Unfortunately, in patients with germline Hh pathway mutations,

75   or intratumoral mutations in *P53*, the five-year overall survival is halved, from 81% to 41% (*7,*

76   *8*). Making matters worse, patients with *P53* mutations often have amplifications in

77   downstream targets like *GLI2* and *NMYC* (*9, 10*), meaning that they will not respond to

78   inhibitors that target the SMO protein.

79 An alternative therapeutic approach is to force tumor cells into terminal differentiation,

80 which can be less toxic than alkylating chemotherapy or radiation (*11-13*) and does not rely on

81 apoptosis or other cell death machinery. The optimal procedure for inducing terminal

82 differentiation is likely to vary from cell type to cell type, since differentiation of neurons

83 depends on different genes than, for example, differentiating blood cells. Neuronal

84 differentiation of MB does occur spontaneously, as it has been commonly observed in human

85 MB pathology specimens for over 30 years (*14-16*). BMP4 induces differentiation of MB cells,

86 reflecting its normal effect on GNPs (*17, 18*). Unfortunately, no pharmaceutical BMP agonist

87 currently exists. Developmental regulation of cerebellar granule neurons potentially provides

88 us with blueprints for engineering a differentiation therapy that is specific to Shh-subtype MB

89 differentiation.

90 GNPs undergo approximately eight symmetric divisions (*19*), during transit amplification in

91 the external granule layer (EGL) (Fig 1A). As GNPs divide they travel inward from the pial

92 surface, eventually exiting the cell cycle. GNP movement, morphogenesis, and synapse

93 formation lasts for about 10 days after cell cycle exit (*20-22*). Following the last mitosis the cells

94 remain in the inner EGL (iEGL) for approximately 48 hours. While in the iEGL the GNs begin to

95 extend two lateral processes, then a deep process (Fig 1B). Each GN nucleus migrates inward

96 through the deep process, along Bergmann glia and past the Purkinje cell layer, into the Internal

97 Granule Layer (IGL). The final shape of a GN is a T, with most of the cell's three processes

98 located in the molecular layer and the nucleus in the IGL. For each step of GNP differentiation,

99 positive and negative regulators have been discovered (*23, 24*). The extensive movement and

100   morphological changes involve the changing expression of hundreds of genes, as shown by

101   recent transcriptional profiling (*25*).

102   We set out to explore epigenetic regulation of genes whose expression increases during

103   differentiation. Many genes whose transcription change during differentiation encode

104   chromatin-remodeling complexes, implying coordination at the level of transcription (*25*). In

105   addition, SHH MB harbor somatic mutations in genes which impact a number chromatin

106   modifying complexes including genes that impact H3 methylation at K27 and K4 (*26*). A

107   mechanism that represses pro-differentiation genes potentially could be inhibited by an anti-

108   cancer drug and would potentially stimulate differentiation of MBs.

109   Our plan was to comprehensively describe histone modifications and critical transcription

110   factors at promoters and enhancers of genes that become active during GNP development, to

111   discover inhibitors of differentiation. We found that more than half of the GNP differentiation

112   genes are associated with histones modified to be H3K27me3 and H3K4me3. H3K27

113   methylation is carried out by the Enhancer of zeste homolog 2 (EZH2) histone

114   methyltransferase, a component of one of the Polycomb Repressive Complexes (PRC2) that

115   were discovered in Drosophila (*27, 28*). H3K4me3 is formed by the MLL complex (*29*) and was

116   not further investigated in our studies. The frequency of H3K27 modifications suggested that

117   inhibition or mutation of EZH2 could lead to premature differentiation, and perhaps to

118   differentiation and growth cessation by MB cells. In *Ezh2* mouse mutants we observed

119   accelerated differentiation of GNPs that had exited the cell cycle. We were able to induce

120   differentiation of MB cells by combining an EZH2 inhibitor with a CDK4/6 inhibitor that arrested

121   cells in G0.

122

Results

Identification of genes activated at the onset of GNP differentiation

We used Percoll fractionation to enrich for GNPs from wild-type mouse cerebella at three key stages, proliferation initiation (P1), peak proliferation (P7), and the onset of differentiation (P14), and then extracted RNA (Materials and Methods; the RNA preparations used are diagrammed in blue in Fig. 1C). We purified earlier-stage GNPs from E15.5 mouse embryos; these had seen little or no Shh (Materials and Methods). E15.5-stage GNPs were also isolated by fluorescence-activated cell sorting (FACS) from E15.5 mice harboring a *Math1-GFP* reporter (*30*). *Math1-GFP* is expressed in neural progenitor cells from the dorsal neural tube, adjacent to the roof plate, that are committed to a GNP lineage. The reporter remains active until GNPs complete their final mitosis.

Data for GNPs from stages later than P14 were obtained using the Translating Ribosome Affinity Purification (TRAP) dataset made available by the Hatten lab (*25*). TRAP data were obtained by purifying mRNA from post-proliferative stages of GNP differentiation (P18, P28) in cells expressing *NeuroD1,* which is transcribed as GNs exit from the cell cycle. TRAP has the benefit of allowing detection and quantification of RNA in the delicate granule neuron processes which are otherwise lost when cerebellar tissue is broken up. *NeuroD1* is not expressed at E15, so earlier time points were not accessible using TRAP. Our RNAseq data were combined with the NeuroD1-TRAP data (23) to achieve a picture of transcription from the earliest stages of GNP formation at E15 to their terminal state at P56.

143   To identify genes that increase transcription during differentiation we followed a multistep

144   process (Fig. 1C). First, genes were excluded if their transcript level was below a cutoff,

145   established using the maximum expression time point of each dataset in both our RNAseq and

146   the Hatten lab TRAP data, and fitting a mixture of two probability distributions to the bimodal

147   data (expressed and unexpressed). Next, we excluded genes that were potentially

148   contaminants from other cell types.   Percoll-fractionated samples from P7 mouse cerebellum

149   typically contain about 95% GNPs and 5% contaminating cells (Fig. 1C, blue v. gray). Genes that

150   are highly expressed in non-GNP cerebellar cells, and scarcely expressed in GNPs, were

151   identified and excluded based upon single-cell RNAseq (scRNAseq) of the developing mouse

152   cerebellum from E10 to P14 (*31*). 1874 genes that were represented by transcripts in bulk

153   cerebellar RNA were determined to be likely contaminants based upon the results of the

154   scRNAseq.   Third, genes that vary substantially during the cell cycle were removed as well.

155   GNP differentiation genes were grouped according to when during development they had

156   maximum transcript abundance. Genes whose transcript levels changed less than 2-fold

157   between developmental stages were categorized as unchanged.

158   2050 genes were most highly represented in RNA between P14 and P56 and were

159   categorized as differentiation genes. Some peaked early in differentiation, and some peaked

160   during maximal GNP proliferation from P1 to P7. We used the time at which a gene's transcript

161   reached 50% of its maximum (t50) to describe when genes were undergoing the most

162   transcriptional changes (Fig S1A-C). If a gene reached 50% of its maximum transcript level

163   before P0 it was set aside. Our focus on differentiation therapy means we are primarily

164   interested in genes that increase after the period of peak proliferation, as this is most similar to

165   MB.

166   787 genes increased 4-fold to 12.4 fold at or after P14, comparing the lowest to highest

167   contiguous time points, and were categorized as differentiation genes (Fig 1C and Supplemental

168   Table 1). Many of the differentiation genes are involved in neuronal function with 181 genes

169   impacting membrane potential or synaptic signalling, which includes 45 ion channels and 45

170   transporters. Genes involved in cell morphogenesis make up another 57 genes including cell

171   adhesion proteins and another 28 proteins involved in the cytoskeleton. In addition to these

172   terminal effectors of building a functional neuron we also see an increase in 50 transcription

173   factors, which could have extensive downstream impact on transcription (Supplemental Table

174   2).

175   Transcripts of a different set of 440 genes were highest (>= 4 fold) during proliferative

176   stages P0-P7. As expected, these proliferation genes included *Gli1,* a direct transcriptional

177   target of the Shh signal transduction pathway that drives GNP proliferation, as well as cell cycle

178   regulators including the G1/S phase cyclin *Ccnd1.* The majority of the genes that have *lower*

179   RNA abundance as GNPs approach cell cycle exit are known regulators or components of the

180   cell cycle such as components of the E2f-Rb complex which controls expression of S-phase cell

181   cycle related genes. Transcript levels for a third set of 783 genes were highest (>= 4-fold

182   change) in the E15 pre-Shh GNPs (*32, 33*).

183   We checked a putative differentiation gene to see if its protein abundance reflected the

184   observed changes in RNA levels. P7 cerebellar sections (Fig S1E) and GNPs differentiated *in*

185   *vitro* (Fig S1F,G) had changes in protein abundance that agree with the RNASeq results. *Cbx7*

186   was among the differentiation genes that had increased transcripts at P14 compared to P7.

187   Levels of Cbx7 proteins increase in the inner EGL and further in the IGL (Fig S1E), where GNPs

188   have recently exited the cell cycle and initiated the first stages of differentiation.

189   GNP division, differentiation, and migration can occur during a wide developmental

190   window, from P3 to P10 (*19*). The densely packed nuclei within the EGL and IGL preclude

191   accurate quantification of protein levels. To avoid these problems we used GNP culture, which

192   permits accurate and automated single-cell quantification. The murine *Math1* bHLH

193   transcription factor was used to distinguish dividing from non-dividing cultured GNPs. *Math1*

194   expression stops when the GNPs stop dividing. *Math-1* reporter GFP (*30*) fluorescence allows

195   classification of GNPs as differentiated or proliferating. To estimate the changes in Cbx7

196   during differentiation in culture we compared 6h Atoh1 high cells (dividing GNPs) to 48 h Atoh1

197   low cells (differentiated GNs). Cbx7 was 3.3 times higher in the differentiated GNs then the

198   dividing GNPs (Fig S1 D-G).

199   The transcription of the 787 differentiation genes varies in the exact timing of transcription

200   activation, as reflected in Fig S1A. A regulator of a set of differentiation genes, among the 787,

201   might be a good target for therapeutic manipulation to force MB cells to differentiate. Based

202   upon gene expression patterns, SHH-subgroup MB cells are highly similar to Shh-exposed

203   dividing P7 GNPs (*31*) . Both cell types rely on Hh signaling as a mitogen (*1*). Mutations of Hh

204   components in the GNP lineage are adequate to induce medulloblastomas (*6*). Further

205   experiments examining epigenetic regulators therefore focused on P7 GNPs.

206 **The chromatin repression modification H3K27me3 is present in P7 GNPs on half the 787**

207 **differentiation genes, and correlates with H3K4me3 and poised RNA Pol2**

208 To gain insight into the transcriptional regulation of differentiation genes, we

209 investigated the chromatin state of P7 GNPs. The positions and abundance of six histone

210 modifications and two chromatin-associated proteins were measured using ChIP-Seq:

211 H3K27me3, H3K27ac, H3K36me3, H3K4me3, H3K4me1, H2Aubi119, Ring1b, and Pol2S5. We

212 selected the histone modifications and known chromatin bound proteins for ChIP based on

213 known markers of promoters, enhancers, and to broadly assess transcriptional repression.

214 Modifications associated with Polycomb-mediated transcriptional repression were mapped,

215 including H3K27me3, which is produced by the PRC2 complex (*34*), H2Aubi119, which is

216 produced by the PRC1 complex (*35*), and Ring1b, which is a core component of the PRC1

217 complex and is the ubiquitin ligase that catalyzes H2Aubi119 modifications.

218 Another form of transcriptional repression employs CpG island DNA methylation. DNA

219 methylation was measured using methylated-CpG island recovery assay (MIRA), which uses

220 recombinant MBD protein to bind double-stranded methylated DNA (*36*).

221 Protein modifications at active promoter regions were assessed, including H3K4me3, S5-

222 phosphorylated RNA polymerase 2 (Pol2S5), (which labels paused RNA polymerase), H3K4me1

223 (which is associated with active enhancer regions), and H3K27ac (which is found at active

224 promoters and enhancers) (*37-40*). DNA accessibility was assessed by ATAC-Seq, which is based

225 upon the bias for Tn5 transposition towards open chromatin (*41*). To quantify the amount of a

226 histone modification at a given gene we quantified the number of reads within 250 BP of the

227 transcriptional start site (TSS). Several of the histone modifications, including the

228 transcriptionally repressive modifications accumulate at the TSS and extend towards the gene

229 body and upstream (Fig S2C,D). This extension of the histone modifications has been shown to

230 be biologically relevant for H3K27ac at super-enhancers (*42*) and for H3K27me3 at permanently

231 repressed genes like Hox genes. To better separate strongly marked genes from moderately

232 marked genes we extended the quantified region to include significantly bound DNA regions

233 farther from the TSS (Materials & Methods).

234 Of all the histone modifications and histone-associated proteins assessed for selective

235 presence with the differentiation genes, the frequent presence of H3K27me3 was most striking.

236 Of the 787 differentiation genes 447 (57%) had H3K27me3 within 250 BP of the TSS (Fig 2B). To

237 identify important modifications we calculated enrichment, meaning the amount of a

238 modification in the 787 differentiation genes compared to the amount in either all genes or in

239 expressed genes during the GNP time-course. H3K27me3 was 2.3 times more frequent near

240 differentiation genes compared to all expressed genes at P7 (p-val 7.54×10^{-147}, hypergeometric

241 BH adjusted) and 2.7 times more frequent compared to all genes (p-val 7.14×10^{-198},

242 hypergeometric BH adjusted) (Fig. 2A). H2Aubi119, a repressive modification made by Ring1b,

243 a component of the PRC1 complex, was also more frequent at the differentiation gene set with

244 2.17 enrichment over all genes (p-val 1.15×10^{-245}, hypergeometric BH adjusted) and 1.89 over

245 all expressed genes at P7 (p-val 3.71×10^{-156}, hypergeometric BH adjusted).

246 The frequent presence of H3K27me3 modifications suggests that PRC2 may repress

247 differentiation genes during GNP transit amplification. The PRC2 complex contains the

248 methyltransferase EZH2, which carries out H3K27 methylation.   From past studies (*43*) we

249 know that PRC2 is present at specific chromatin regions, where it functions as a transcriptional

250 repressor. The amount of H3K27me3 present regulates whether repression is temporary

251 (moderate levels) or permanent (high levels) (*44-46*). The differentiation genes have a

252 moderate amount of H3K27me3 (Fig S2A-C). Only three differentiation genes had high levels of

253 H3K27me3. The other, non-differentiation, genes within the high H3K27me3 group included

254 Hox cluster and transcription factors associated with alternative fates or earlier lineages. As an

255 example, *Cbx7*, a differentiation gene, has moderate K27me3 while Lhx9 and Hoxa10 have high

256 K27me3 (Fig SC). Very highly H3K27me3-modified genes are thought to be permanently

257 repressed (*47*).

258 In addition to the amount of H3K27me3, whether PRC2 repression is transient or long-

259 lived depends on its association with other histone marks or protein complexes. For example,

260 H3K27 methylation may occur in association with active-gene modifications such as H3K4me4

261 and/or poised RNA polymerase II (*48*). This kind of arrangement is known as a bivalent

262 promoter, transcriptionally repressed but poised for increased transcription (*49, 50*). In

263 contrast, PRC2 can establish more permanent repression when associated with certain PRC1

264 variants (*51*). However, these are heterogeneous complexes, and changing select PRC1 subunits

265 allows the association with bivalent promoters as well (*52*). H3K27me3 can recruit the

266 machinery for DNA methylation (*53*), driving permanent repression.

267 To distinguish possible roles of PRC2 in GNPs we examined the relationship between

268 H3K27me3 and H2Aubi119 (a marker of PRC1 complex) or H3K4me4 (a marker of active

269 promoters) at differentiation genes that have H3K27me3. H3K27me3-marked differentiation

270 genes have both H3K4me3 and PRC1 complex (H2Aubi119). DNA methylation was detected in

13

271   only 4 percent of differentiation genes, indicating that this form of repression is mostly not

272   active there.

273   The association of H3K27me3 with other modifications at differentiation genes is

274   represented as a chart (Fig 2B). Each modification is represented by a column that shows the

275   numbers of modified and unmodified genes. The columns are organized from left to right

276   according to the number of genes that are also marked by H3K27me3. The red band shows

277   genes containing H3K27me3 which share other modifications. Of the 447 H3K27me3-marked

278   differentiation genes, 87 % also had H3K4me3 and 84.3% had paused RNA polymerase. PRC1

279   occupancy on the H3K27me3-bound differentiation genes was frequent: 89 % of the 447 genes

280   had significant H2Aubi119. The frequent associations between H3K27me3 and H2Aubi119 or

281   H3K4me3 are also seen with a scatter plot (Fig S2 D,E), where 373 (83%) of the differentiation

282   genes bear all three modifications.

283   Thus at P7 many of the 447 differentiation genes had nearby PRC2 complexes, PRC1

284   complexes, and markers of active promotors such as H3K4me3 and RNA Pol2Ser5P (paused

285   RNA polymerase 2). These results suggest that about half of the differentiation genes have

286   bivalent or poised promoters containing both PRC2 and PRC1. Removal of these modifications

287   in the normal course of development, or engineered removal in MB cells, may cause de-

288   repression of these genes and early differentiation.

289   **Ezh2-mediated H3K27 methylation delays differentiation of GNPs**

290   The H3K27me3 histone modification, associated with gene repression, is enzymatically

291   carried out by the protein complex PRC2. The presence of H3K27me3 modifications at 447 GN

14

292   differentiation genes at the P7 stage suggests that PRC2 may be blocking differentiation. In

293   that case differentiation of GNs, or perhaps MBs, would require relief from PRC2 repression.

294   We tested this hypothesis using mice carrying a mutation in *Ezh2*, which is the enzymatic

295   component of PRC2 that catalyzes formation of H3K27me3. Homozygous *Ezh2* knockout mice

296   die as embryos (*54*), so studying postnatal cerebellar development required conditional

297   knockout mice. Mice with LoxP sites flanking the DNA encoding the SET domain of *Ezh2* (*55*)

298   were crossed with *Math1-Cre* mice (*56*). The SET domain is required for Ezh2 to function as a

299   methyltransferase (*57*) and maternal depletion of the SET domain in mice causes significant

300   growth retardation (*58*).

301   As a consequence of crossing the *Ezh2* Lox-P mice with the *Math1-Cre* mice, H3K27me3 is

302   reduced in the granule neurons (Fig S3 A-C). *Ezh1*, a paralog of *Ezh2* that is present throughout

303   GN development is a weaker methyltransferase than *Ezh2* (*59*). Even with *Ezh1* functioning,

304   conditional loss of *Ezh2* led to dramatic loss of H3K27me3 from GNPs and GNs, as shown in P7

305   cerebellar slices (Fig S3 A panel II vs VI, yellow arrow) and cultured GNPs (Fig S3 C panel II vs IV,

306   yellow arrow).

307   The most notable phenotype of the *Ezh2* cKO mice is a blurring of the boundary between

308   the inner external granular layer (iEGL) and the molecular layer (ML; Fig 3B-C, magenta and

309   cyan arrow). GNs within the inner EGL (iEGL) permanently exit the cell cycle and remain there

310   as they extend parallel fibers. GNs within the iEGL express the cell cycle inhibitor p27. In the

311   *Ezh2* cKO the iEGL is more diffuse and blends into the ML (Fig 3A compare cyan arrows). To

312   facilitate quantification of the EGL blurring we collapsed 2D fluorescent images into line

15

313   segments (Fig 3D).   P7 cerebellar slices were stained with anti-p27 to label post-mitotic EGL

314   cells, NeuN antibody to identify the IGL, and DAPI to mark all nuclei. For each channel,

315   measurements were made along a line from the pial border on the outside to the IGL. The 581

316   lines (266 WT and 315 *Ezh2* cKO) were aligned and averaged, in sets according to genotype (Fig

317   3E). The normalized p27 intensities show a spreading of iEGL, blurring the boundaries with the

318   IGL and ML. The ML blurring, was quantified as an increase in the p27 at the junction of the

319   iEGL and ML in the *Ezh2* cKO (Fig 3D; compare the cyan arrows). To quantify across replicates,

320   we compared *Ezh2* cKO and WT at a point within the ML where the *Ezh2* cKO had the highest

321   relative p27 fluorescence (Fig 3E).

322   The sizes of the layers of the cerebellum are largely unaffected by *Ezh2* cKO (Fig 3G,H). **T**he

323   different layers of the cerebellum were measured in slices stained with anti-p27, NeuN

324   antibody, and DAPI (Fig. 3F). No significant differences were observed in the thicknesses of the

325   oEGL, iEGL, ML, or IGL (Fig 3G,H). Due to the diffuse EGL/IGL-ML boundary in the cKO, p27

326   fluorescence intensities within the iEGL (where GNPs begin differentiation) and IGL (where

327   post-mitotic GNs reside) were reduced 25% and 23% (Fig 3I). These findings are consistent with

328   the loss of *Ezh2* function not altering the overall structure of the cerebellum, but instead

329   specifically affecting GN differentiation.

330   *Ezh2 cKO*- GNPs labeled with a 48 h EDU pulse migrated from the EGL prematurely (Fig.

331   S3 D-F). To distinguish early migration out of the oEGL from stalled GN migration within the

332   ML, GNPs going through S-phase were labeled with EDU and harvested 48 hours later. In WT

333   mice there is dense EDU labeling of the iEGL, and GNs lining up along the border with the ML

334   (Fig S3 D, panel III versus VIII, yellow arrows). In the *Ezh2* cKO, EDU-labeled cells are within the

335   diffuse iEGL and within the ML (p-val 0.024), mirroring what was seen with p27

336   immunofluorescence (Fig S3E,F). We conclude that, in *Ezh2* mutant mice, GNs prematurely exit

337   from the EGL into the ML, a movement typical of wild-type GNs that have stopped dividing.

338   The hypothesis that PRC2 blocks cell differentiation is consistent with the *Ezh2* mutant results,

339   because early de-repression of differentiation genes would cause premature EGL cell migration.

340   GNPs cultured from *Ezh2* cKO mice, compared to normal, had more differentiated cells but

341   the same fraction of dividing cells. That fits with the idea that loss of *Ezh2* allows premature

342   activation of differentiation genes. To further test the impact of *Ezh2* cKO on differentiation,

343   we cultured GNPs with Shh and monitored *Map2* (Fig. 4A,C), a marker for process extension,

344   and *NeuN*, a marker of differentiated GNs. Process extension was measured using Neuroncyto

345   2 (*60*), which reveals cell processes and assigns them to a cell body (Fig. 4B,D). *Ezh2* cKO GNPs

346   had a 37.6% increase (p-val 0.007) in average process length compared to control (Fig 4E).

347   Next, we separated the cells into groups based upon process length (Fig 4F). WT cells had a

348   19.2 % higher proportion of cells with no process (49.2 % WT vs. 30% in *Ezh2* cKO; p-val 0.019)

349   or a process less than 5 pixels long (p-val 0.0047).   *Ezh2* cKO cells had processes 10 pixels and

350   longer 20.1% more often (39.3 WT versus 59.4 *Ezh2* cKO). Thus loss of *Ezh2* led to more of the

351   longer processes, an indicator of differentiation, in cultured GNPs.

352   Cell cycle stage and differentiation were quantified using staining for DAPI (to show all

353   nuclei), Ki67 (to show dividing cells), and NeuN (to show post-mitotic neurons) (Fig S4A). The

354   fraction of total cells that were NeuN-positive in *Ezh2* cKO cultures was 13.9 % compared to 9.8

355   % in WT (p-val 0.008) (Fig S4C). The amount of NeuN fluorescence increases on the per-cell

356   histogram (Fig S4B). No significant change in the number of cells that were in G1 (p-val 0.107)

357   or G2 (p-val 0.087) occurred, with cells more often being in G1 in *Ezh2* cKO and in G2 in WT (Fig.

358   S4C). *Ezh2* appears to be a cell-intrinsic regulator of differentiation timing; its loss hastens

359   process extension and nuclear migration out of the EGL.

360   **During normal development, *Ezh2* transcript and protein levels decrease as GNPs**
361   **differentiate**

362   Reduced PRC2 activity as GN differentiation commences could be due either to reduced

363   Ezh2 protein levels or to functional inactivation. Among genes encoding components of

364   repressive chromatin complexes, transcript levels for *Ezh2* and *Cbx7* changed the most during

365   early GN development, with *Ezh2* transcript being reduced 8.8 fold after P7 (Fig 5A,B). GNP cell

366   cycle exit coincides with a reduction in Ezh2 protein level, as shown by reduced staining

367   intensity in the iEGL (Fig 5C). To further explore this observation, P7 GNPs freshly isolated from

368   *Math1>GFP* reporter mice were plated to observe differentiation. As early as 6 hours after

369   plating, the average level of Ezh2 was lower in GNs that had begun to differentiate, as

370   determined by low Math1-GFP levels. Relative fluorescence for Ezh2 continued to drop at 24

371   hours of culture (Fig 5D). Thus cell cycle exit strongly correlates with decreased Ezh2 levels in

372   cultured cells and in vivo.

373   The results so far suggest that Ezh2-based H3K27me3 modifications at promoter regions

374   delay transcription of many differentiation genes during GNP proliferation. Once GNPs

375   complete their final mitotic division and enter G0 in preparation for differentiation, reduced

376 *Ezh2* function may foster activation of the GN differentiation program. Can this knowledge be

377 applied to manipulate MB cells?

378 **Medulloblastoma cells also H3K27-trimethylate GN differentiation genes**

379   In MB cells, as in dividing GNPs, repressive chromatin regulators may prevent expression of

380 GN differentiation genes to maintain a pro-proliferative state. Indeed, 95% of the 447

381 differentiation genes that are H3K27-marked in GNPs are repressed in MB cells compared to

382 GNs (Fig 6C). To determine whether GN differentiation genes are stably repressed in MB, we

383 measured chromatin markers and mRNA transcript abundance in MB samples from *Ptch1$^{+/-}$*

384 mice. *Ptch1* encodes the Hedgehog receptor, a negative regulator in the pathway, so in these

385 mice, and in humans with the same kind of mutation, derepressed Hedgehog target genes

386 increase the frequency of MB. RNAseq was used to compare transcript populations in MBs

387 from *Ptch1$^{+/-}$* mice to P1, P7, and P14 GNPs. As expected, MB transcripts correlated most with

388 transcripts from rapidly dividing P7 GNPs (R^2 = 0.79) compared to P1 (R^2 = 073 , Fig S6 B) or P14

389 (R^2 = 0.52, Fig S6 C).

390   In MB cells, three-quarters of the GN differentiation genes have H3K27me3 at their

391 promoters (Fig S6 A,C). The Pearson correlation between MB cells and P7 GNPs was also

392 strong for histone markers, with H3K27me3 being 0.79, H2Aubi119 being 0.87 and H3K4me3

393 being 0.95 (Fig. S6A). Among genes that increase expression during GN differentiation, only

394 27% of the H3K27-methylated GN differentiation genes did not have H3K27me3 in MB cells (Fig

395 6 A,C).   The majority of GN differentiation genes are persistently repressed in MB.

In human SHH-subtype medulloblastomas, higher levels of *EZH2* transcript correlate with lower-level expression of GN differentiation genes

The inverse relationship between GN differentiation gene transcription and Ezh2 levels holds true in human MB tumors as it does in mouse MBs and developing mouse cerebellum. The levels of *EZH2* transcription from 223 primary human samples of *SHH*-subtype MB (*9*) were compared to the levels of GNP differentiation gene transcripts. Samples were ranked in terms of *EZH2* mRNA level (Fig 7A). The 30% of the tumors with the least *EZH2* RNA were compared to the top 30% (Fig S7A). GN differentiation gene transcript levels were on average 1.3 fold higher in tumors with low EZH2 transcript than in tumors with high EZH2 (Fig S7A).

Comparing human genes that were differentially expressed in *EZH2*-high vs *EZH2*-low SHH MB samples with the expression of their mouse homologs revealed a striking pattern (Fig 7B). Genes that were significantly more highly transcribed in human MBs that had relatively low *EZH2* RNA were 26-fold enriched for genes whose transcription increases during mouse GNP differentiation (Fig 7C). 60% of the human genes that had low expression when *EZH2* RNA was high were among the mouse GNP differentiation genes (343/570). The amount of Ezh2 transcript in each individual tumour was also anticorrelated with the transcript levels of the individual differentiation genes (Fig S7B,C). The average Pearson correlation for the differentiation genes was -0.24 indicating a negative correlation (Fig S7B,C). Thus the relationship between *EZH2* transcription and differentiation gene transcription is maintained in human MBs.

416   Patients with high *EZH2* RNA tumors had significantly worse 5-year (*EZH2*-high 73% versus

417   *EZH2*-low 91%) and 10-year (*EZH2*-high 64% versus *EZH2*-low 84%) survival (Fig 7D), so patients

418   with lower *EZH2* RNA and more differentiation gene expression have a better prognosis.

419   **Combined Ezh2 inhibitors and CDK4/6 inhibitors force MB cells to undergo neuronal**

420   **differentiation**

421   Mouse MB cells isolated from *Ptch1*$^{+/-}$ mice (*61*) were plated on laminin-coated plates and

422   cultured for 72 hours in serum-free medium, with or without small molecule inhibitors (Fig 8A).

423   We measured rates of proliferation and differentiation using 2 combinations of antibodies and

424   dyes. In one type of experiment, we used anti-pRb (Ser807/811) to label G1/2 versus G0 and

425   NeuN to label differentiated cells (Fig 8A,B). In a second type of experiment, the antibody

426   combination was p27, which identified quiescent G0-arrested MB cells, and Atoh1, which is

427   only present during MB proliferation (Fig S8A,B). Cycling MB cells have high Atoh1 and low p27

428   if in G1/S/G2 (green in Fig. S8A) or high p27 if in G0 (yellow in Figure S8A). Cells embarking on

429   differentiation (red in Fig. S8A) have high p27 but relatively low levels of Atoh1. NeuN marks a

430   later stage of development than p27 presence or loss of Atoh1.

431   Untreated MB cultures had 70.2/43.6% (pRb high / Atoh1 high p27 low) dividing cells and

432   2.0/14.2% (NeuN high / Atoh1 low p27 high) differentiating cells. Cultures treated with Ezh2

433   inhibitor (5 uM UNC1999) had 50.4/18.6% (pRB high /Atoh high p27 high) dividing cells and 4.6/

434   35.2% (NeuN high / Atoh1 low p27 high) differentiating cells (Fig 8B, Fig S8B). Ezh2 inhibition

435   caused a 21 % increase in the fraction of differentiated cells, based upon measuring Atoh1 and

436   p27 (p-val < 0.001) and a 2.6 % increase in NeuN positive cells (p-val < 0.001). For UNC1999,

437   previous studies of cultured cells showed that a dose of 1 to 5 uM caused substantial reduction

21

438   in H3K27me3 activity without substantial toxicity (*62*). Thus induction of differentiation genes

439   using Ezh2 inhibitor reduced but did not stop MB cell growth, in keeping with a lack of effect on

440   MB frequency due to genetic removal of Ezh2 function. *Ptch1*$^{+/-}$ mice were crossed with *Ezh2*$^{fl/fl}$

441   Math1-Cre mice. About 15% of the *Ptch1*$^{+/-}$ mice develop MBs. *Ezh2* cKO did not affect the rate

442   of MB formation in *Ptch1*$^{+/-}$ mice.   MB formation occurred in 14.86% (n = 74) who were Cre$^{+/-}$

443   and 14.28 % (n = 84) in Cre$^{-/-}$ animals.

444   Normal development may be informative about how to stop MB cells from growing. During

445   normal differentiation, GNPs would first enter G0 arrest, then GNP differentiation genes would

446   be de-repressed as Ezh2 is reduced. To stop MB cell proliferation, the same two steps might be

447   required: going into G0 arrest and then differentiating.   MB cultures treated with CDK4/6

448   inhibitor (1 uM Palbociclib) to drive them into G0 (*63*), had 18.1/15.4% (pRb high / Atoh high

449   p27 low) dividing cells and 15.9/26.0 % differentiating cells (NeuN high / Atoh1 low p27 high).

450   Thus an inhibitor that pushes MB cells toward G0 is does increase rates differentiation more

451   than the Ezh2 inhibitors alone but still at relatively low rates (Fig 8B, Fig S8B).

452   Dual treatment with Ezh2 inhibitor and CDK4/6 inhibitor produced the highest percentage

453   of terminally differentiating MB cells 22.8/43.0 % (NeuN high / Atoh1 low p27 high) with only

454   9/6.8 % (pRb high / Atoh1 high p27 low) percent of cells dividing (Fig 8B, Fig S8B). The

455   combination of Ezh2 inhibitors and CDK4/6 inhibitors increased the rate of differentiation by

456   7% for NeuN positive cells (p-val 0.004) and 17% for low of Atoh1 with high p27 (p-val < 0.001).

457   MB cells treated with both 5uM UNC1999 and 1um Palbociclib developed thin neuron-like

458   processes, that contain the F-actin stain phalloidin (Fig S8B xiii). In contrast, after treatment

22

459   with CDK4/6 inhibitor alone, no such processes were observed and the cells appeared similar to

460   dividing MB cells (Fig S8B x). It should be noted that differentiated GN require changes to the

461   media for long term survival which could limit the time an MB cell could survive late into

462   neuronal differentiation.

463   Combining a CDK4/6 inhibitor with an Ezh2 inhibitor could be toxic to dividing cells. The

464   increase in percentage of differentiated cells would then reflect more robust survival of

465   differentiated cells vs proliferating cells. If selective survival explained the results, then the

466   absolute number of differentiated cells should be similar in untreated and doubly treated cells.

467   Instead, combining 5uM UNC1999 and 1 uM Palbociclib produced 2.2 to 4.68 times more

468   differentiated cells compared to control cells not treated with any drug (Fig S8C). This suggests

469   that combining Ezh2 and CDK4/6 inhibitors drove conversion of dividing cells into differentiated

470   cells, rather than causing selective death of dividing cells.

471   A key advantage of differentiation therapy over anti-proliferative approaches is that

472   terminally differentiated neurons should not re-enter the cell cycle even after the treatment is

473   terminated. MB cells in culture were treated with 1 uM of the CDK4/6 inhibitor alone or in the

474   presence of various doses of Ezh2 inhibitor. After 72 hrs, all drugs were washed out and the

475   cells cultured for an additional 24 h (Fig. 8C). As previously, cells were labeled using anti-pRb

476   (Ser807/811) and NeuN (Fig. 8D). When CDK4/6 inhibitor was used alone, following drug wash

477   out 40.8 % of MB cells re-entered the cell cycle (Fig 8E).   Thus, with only CDK4/6 inhibition, MB

478   cells can rapidly re-enter the cell cycle. Only 14.2 % of cells treated with both inhibitors re-

479   entered G1/2. Again, we saw an increase fraction of differentiated from 14.5 % of cells to

23

480   21.9% (p-val 0.006) (Fig 8E) and in the total number of differentiated cells by 1.68 times (p-val

481   0.016) comparing dual Ezh2 and CDK4/6 inhibitors compared to CDK4/6 inhibitors alone (Fig

482   S8D). The combination of Ezh2 inhibitors with CDK4/6 mediated cell cycle arrest achieves the

483   most important therapeutic goal, to irreversibly prevent cell cycle re-entry.

Discussion

484   The parallels between early cerebellar development and MB formation provide an

485   opportunity to study key regulators of normal development in the context of tumor cells, with

486   the goal of stopping tumor growth. During normal cerebellar development, GNPs proliferate

487

488   under the mitogenic effect of the Sonic hedgehog pathway. Following a period of transit

489   amplification, GNPs exit the cell cycle and terminally differentiate into granule neurons, the

490   most abundant neuron in the brain (Fig 1). In MBs, the SHH pathway is aberrantly activated

491   through mutations that inactivate inhibitory elements of the pathway (eg Patched or Sufu) or

492   through amplification of activating elements (eg *Gli2* amplification). As a result, cells fail to exit

493   the cell cycle and can ultimately give rise to a tumor. A large body of evidence describes the

494   morphological (*64*), transcriptional (*65*), and post-translational modifications (*66*) similarities

495   between transit-amplifying GNPs and medulloblastomas.

496   **Ezh2-mediated H3K27me3 broadly represses differentiation genes in GNPS and MBs**

497   Here we undertook a genome-wide identification of the epigenetic regulators and

498   transcriptional changes that occur during the initiation of proliferation, peak proliferation, and

499   early stages of differentiation in GNPs.   In agreement with other groups, we find that many

500   genes whose transcription increases as GNPs differentiate have bivalent promoters, with

501   H3K27me3 and H3K4me3 modifications (*67, 68*). Our study also shows PRC1 occupancy at the

502   majority of the H3K27me3-marked differentiation genes (Fig 2). Most PRC1 complex variants

503   and the PRC2 complexes are involved in transcriptional repression, which allows a transient

504   repression of genes required during differentiation. The roles of PRC2 and PRC1 complexes

25

505 during differentiation has been well described in many different cell types including other types

506 of neurons (*69*), myocytes (*70-72*), cardiomyocytes (*73*) and T-cells (*74*).

507 **Bivalent H3K27me3 and H3K4me3 modifications delay transcription of specific gene sets**

508 **during GNP cell cycle exit**

509   For a cell with complex cytoarchitecture like a neuron, it is important to turn on the correct

510 genes during differentiation and to have those genes turn on at the correct time. Ezh2 is

511 transcriptionally activated by the pRb/E2f1 complex during S-phase expression(*75, 76*). In GNPs

512 the bivalent H3K27me3 and H3K4me3 modifications mark a subset of genes that appear to be

513 sensitive to the drop in Ezh2 function. The subsequent transcriptional activation of genes

514 associated with neuronal differentiation, like ion channels, can in this way be reliably linked to

515 cell cycle exit. The reduction of Ezh2 protein (Fig 5) that occurs as GNPs complete their cell

516 division stage is likely to promote terminal cell cycle exit by allowing de-repression of

517 differentiation genes.

518   What determines the exact timing of transcriptional activation for a given differentiation

519 gene is likely multifactorial. Kdm6b, an enzyme that removes H3K27me3 methylations,

520 significantly influences timing during GNP differentiation (*77*). The abundance of Kdm6b across

521 the H3K27me3 marked differentiation genes may be non-uniform, activating some genes

522 earlier than others. The PRC1 complex has numerous variants, which could fine tune the

523 required delays in GNP differentiation gene expression timing.   Another path of H3K27me3

524 elimination can be replicative dilution, where H3K27me3 modifications are depleted by ongoing

525 cell division following Ezh2 activity reduction (*45, 46*). In GNPs, the drop in *Ezh2* expression

526   happens as cells exit the cell cycle, so replicative dilution does not seem to be an important

527   factor.

Ezh2 loss accelerates differentiation but only after cell cycle exit

529   *Ezh2* cKO allowed early differentiation of GNPs but did not have an impact on transit-

530   amplifying GNPs. During GNP cell division, Ezh2 is highly expressed. As Ezh2 levels drop

531   following cell cycle exit, GNPs activate H3K27me3 modified genes. Premature removal of Ezh2

532   should cause early and/or prolonged activation of differentiation genes. Our *Ezh2* knockout did

533   result in early differentiation but only after the period of transit amplification was complete (Fig

534   3). In cultured GNPs, *Ezh2* cKO did not reduce the number of G1/2 cells. If anything, there was

535   an increase in the number of G1 cells (Fig 4). The phenotype of the *Ezh2* cKO is quite subtle; a

536   previous study did not report a phenotype in the cerebellum in *Ezh2* cKO (*78*). We too found it

537   difficult to observe and quantify the changes to the iEGL. We were alerted to the phenotype by

538   automated analysis of GNP cultures from *Ezh2* cKO mice that revealed increased process

539   extension pointing our attention to the iEGL.

H3K27me3-marked differentiation genes have known GN differentiation phenotypes

541   Many H3K27me3-marked differentiation genes have known neuronal differentiation

542   phenotypes in cerebellar GNs. One important example is the voltage-gated Ca^{2+} channel genes,

543   which have been linked to GN migration. Of the six channel genes that increase transcription

544   during differentiation, five are modified by H3K27me3. Loss of function of these genes impairs

545   normal GN differentiation. Knockout of *Cacna1a* which codes for Cav2.1 showed clear

546   migration defect in the EGL, with persistence of the EGL at P21 (*79*). Another potent regulator

27

547 of Ca^{2+} that is critical to GN migration is the NMDA receptor (*80*), which is a ligand-gated

548 glutamate channel. The genes for all four NMDA subunits that transcriptionally increase

549 (NR2BA-D), are modified by H3K27me3. Functional NMDA receptors form when the radially

550 migrating GNs start migrating into the ML (*81, 82*). NMDA receptors undergo subunit switching

551 between migrating and post migratory receptors (*83, 84*).   Genetically altering subunit

552 composition leads to an increased rate in migration (*85*) and persistent EGL (*86*), while blocking

553 NMDA receptors reduces migration(*87*). The targets of Ezh2 have developmental phenotypes,

554 and the timing of their production matters.

555 Bdnf and multiple CAMK components that transduce its signal are also H3K27me3-modified.

556 BDNF signaling is a well-established regulator of GN radial migration. The knockout of *Bdnf* (*88,*

557 *89*) or of its downstream pathway components *CaMKKII* or *CaMKIV* (*90*) all cause GN migration

558 defects. The opposite phenotype occurs in response to over-activation of the Bdnf pathway,

559 decreasing the time to differentiation. Transfection of GNPs with a constitutively active CREB,

560 the terminal transcriptional activator of BDNF signaling, accelerated terminal differentiation of

561 GNPs in culture (*91*).

562 From a differentiation therapy perspective, not all differentiation genes are equal. The

563 greatest interest lies with genes that could be activated to prevent subsequent re-entry into the

564 cell cycle. Attempted cell division in differentiated neurons typically leads to cell death as seen

565 with neurodegenerative disease (*92-95*) or to binucleated cells as seen with gangliogliomas (*96,*

566 *97*). Our present results suggest several candidate differentiation genes, but another approach

567 is to manipulate Ezh2 directly and thereby control many of these genes simultaneously.

28

568 **Ezh2 inhibitors as a potential differentiation therapy**

569   EZH2 inhibitors have been tested in SHH-subtype MB cells and have caused decreased cell

570 viability (*98, 99*) and increased rates of differentiation (*100*). One rationale for using Ezh2

571 inhibitors in MB was that forced expression of *NeuroD1* in MB cells is capable of driving

572 differentiation (*100*). ChIP qPCR analysis had demonstrated that *NeuroD1* is marked by

573 H3K27me3, and Ezh2 inhibitors showed increased rates of differentiation both in culture and in

574 vivo models**.** Therefore, EZH2 inhibition might derepress *NeuroD1* and spur differentiation of

575 MB cells.

576   Our data provide genome-wide context for the previous work by identifying the large

577 number of H3K27me3-modified genes during development and in MB cells.   EZH2 drives

578 H3K27me3-mediated repression in *NeuroD1* and in more than half of the 787 genes whose

579 transcription increases in early GN differentiation. The mechanism by which EZH2 inhibition

580 promotes cell death and differentiation of MB cells is likely to depend on its regulation of many

581 genes in addition to repressing *NeuroD1*.

582 **Combined Ezh2 inhibition and cell cycle arrest as a differentiation therapy**

583   A prevailing hope is that properly stimulated differentiation can override tumor cell

584 proliferation, for MB and other cancer types (*101-103*). Differentiation therapy in acute

585 promyelocytic leukemia using retinoic acid (RA), has dramatically extended survival of PML

586 patients (*104, 105*). RA induces the cancer cells to differentiate from a granulocyte precursor

587 into a mature myelocyte that can no longer divide (*106, 107*). Given its transformative effect in

588 AML, RA was trialed for patients diagnosed with MB in hopes of similarly driving differentiation

589 and long-term regression. Unfortunately, RA did not prove effective in MB and phase 2 trials

590   were ultimately halted. RA does cause growth arrest of MB tumous (*108, 109*), but through

591   apoptosis rather than induced differentiation (*110, 111*).

592   Our work suggests a nuanced relationship between proliferation and differentiation in GNPs

593   and MB cells. Ezh2 appears to have a significant role in delaying activation of differentiation

594   genes but *Ezh2* loss or inhibition is not capable overriding the cell cycle. *Ezh2* cKO did not

595   reduce GNP proliferation (Fig 3) and there was only a marginal increase in differentiation with

596   Ezh2 inhibition alone (Fig 8). Neuronal differentiation is a complex process and understanding

597   where and how a given regulator fits into that process is critical to maximizing its use as a

598   clinical differentiation therapy.

599   Additional observations raise concerns about using EZH2 inhibitors as a solo differentiation

600   therapy. First, *Ezh2* cKO did not prevent MB formation in mouse models of MB.   SmoM2 mice,

601   who develop MB from unrestrained Hh signalling were crossed with Math1-Cre / Ezh2fl/fl

602   developed MB at 100% penetrance as in normal SmoM2 control mice.   The MBs from the *Ezh2*

603   cKO mice were more aggressive than control SmoM2 with intact *Ezh2*, leading to early death of

604   the mice (*78*). *Ezh2* cKO, in Ptch1$^{+/-}$ mice also showed no impact on the rate of MB formation.

605   The reduction in H3K27me3 with *Ezh2* cKO is substantial, exceeding what is possible with an

606   Ezh2 inhibitor, so using Ezh2 inhibitors alone is unlikely to yield differentiation rates high

607   enough to reduce cancer progression. Another concern is that *Ezh2* cKO has no apparent effect

608   on proliferating GNPs. If anything, there were increased numbers of GNPs in G1 in *Ezh2* cKO

609   mice compared to WT mice, indicating that GNPs will not cease dividing when H3K27me3 is

610   strongly depleted.   Because MB cells are dividing too, Ezh2 inhibition alone will probably not

611   drive a high rate of differentiation.

612   With regards to forced G0 arrest in MB cells, our observations parallel long term animal

613   experiments, where CDK4/6 inhibitors were used with xenografts of human MB cells. The

614   tumors dramatically regressed when mice were treated with inhibitor (*112*), but three-quarters

615   of the tumors recurred within 60 days of drug removal. This suggests that forced exit of the cell

616   cycle is not sufficient to drive terminal differentiation of MB cells. In our experiments, wash-

617   out of Ezh2 and CDK4/6 inhibitors resulted in cell-cycle re-entry of MB cells within 24 hours (Fig

618   8). When developmental regulation was closely recapitulated using dual inhibitors, driving both

619   exit from the cell cycle and inhibition of Ezh2, we observed significantly higher levels of

620   terminal differentiation without re-entry into the cell cycle following drug wash out.

621   **Barriers to clinical differentiation therapy**

622   Our results suggest two critically important ideas for designing a differentiation therapy for

623   MB. First, our evidence supports the use of Ezh2 inhibition as a strategy for the differentiation

624   of Shh-subgroup medulloblastoma (*100*). The second is that premature transcriptional de-

625   repression by Ezh2 inhibition is not sufficient to cause differentiation in a dividing MB cell. Prior

626   to larger scale testing in animals, more extensive work needs to be done to optimize the

627   duration of cell cycle arrest. A phase I trial of Palbociclib for pediatric brain tumours was

628   recently completed which showed bone marrow suppression at higher doses (*113*). One

629   advantage of differentiation therapy is that the cells may not need to be G0 arrested for more

630   than 72 hours to get induction of differentiation, which means the CDK4/6 inhibitor could be

631   delivered in short pulses. As bone marrow suppression took weeks to months to develop these

632   short pulses will prevent accumulated toxicity (*114*). Continuous administration of an Ezh2

633   inhibitor would be supplemented with 72 hour cyclic period of CDK4/6 inhibition.

31

634

Materials and Methods

Crosslinking Chromatin immunoprecipiation (ChIP)

The ChIP protocol was adapted from an existing protocol (*115*). Briefly, a single cell

suspension of GNPs or MB cells were crosslinked with 1% formaldehyde for 10 min, then

quenched with 2.5 M Glycine. Chromatin was sheared using a Bioruptor (Diagenode, Denville,

New Jersey) for 6 cycles of 15 minutes (30 sec on, 30 seconds off at maximum power).

Following sonication the insoluble material was pelleted. Antibodies were added to the

sheared chromatin as indicated by table 1 to 750 ul of chromatin and incubated at 4 C

overnight.   For each ChIP-seq experiment 3 technical replicates of the immunoprecipitation

were performed and pooled after DNA isolation. Protein G agarose beads (Roche) were used to

precipitate the antibody bound protein and 4 sequential washes were done with the buffers

described in the original paper (*115*). Protein was eluted of beads with 10 mM EDTA and 1%

SDS and the DNA was liberated from protein using Proteinase K (Roche). The DNA was purified

using phenol chloroform extraction then treated with RNAse A. DNA was quantified using

Qubit DNA HS (Invitrogen). ChIP-seq libraries were prepared using NEBNext ChIP-Seq Library

Prep (New England Biolabs). Sequencing was performed using HiSeq 2500 (Illumina Inc) with 40

BP single end reads.

654 **Native ChIP**

655   The crosslinking protocol described above was performed for all antibodies in Table 1,

656 except the H2Aubi119 antibody where native ChIP was used. The protocol for native ChIP has

657 previously been described (Hasegawa et al., 2016). In brief, cell lysate from fresh frozen GNPs

658 or MB was incubated in MNase for 20 min at 4°C and stopped by adding 1/25 0.5 M EDTA. The

659 amount of MNase used for each reaction was batch adjusted to obtain mono-nucleosomes

660 after a 20 min digestion. After centrifugation at 13000 rpm for 15 min at 4C, the supernatant

661 containing the mononucleosome fraction was collected. Protein was precipitated using Protein

662 G Dynabeads (Invitrogen), with rabbit anti-IgM IgG linker antibodies for the H2Aubi119 ChIP.

663 The beads were washed 3 times using buffers described in Hasegawa et al (2016). DNA was

664 eluted, freed from protein using Proteinase K (Roche), and purified using phenol chloroform

665 extraction. Preparation of ChIP-seq libraries was performed as described for crosslinking ChIP.

33

666   *Table 1*: Antibodies and concentrations used for ChIP

Antibody	Vendor	Species	Serotype	Catalog	Amount (ug, ul) in 750 ul lysate	RRID
H3K4me3	Abcam	Rabbit polyclonal	IgG	ab8580	5 ug	*AB_306649*
H3K4me1	Abcam	Rabbit polyclonal	IgG	ab8895	5 ug	*AB_306847*
H3K27me3	Milipore	Rabbit polyclonal	IgG	07-449	5 ug	*AB_310624*
H3K27ac	Abcam	Rabbit polyclonal	IgG	ab4729	5 ug	*AB_2118291*
Ring1b	Active Motif	Rabbit monoclonal	IgG	39664	10 ul	*AB_2615006*
H2Aubi119	Milipore (Upstate)	Mouse monoclonal	IgM	05-678	10 ug	*AB_309899*
H3K36me3	Abcam	Rabbit polyclonal	IgG	ab9050	5 ug	*AB_306966*
RNA polymerase 2 (S5 phospho)	Abcam	Rabbit polyclonal	IgG	ab5131	5 ug	*AB_449369*
RNA polymerase 2 (S5 phospho)	Active Motif	Mouse monoclonal	IgG	39097	10 ul	*AB_2732926*

667

668

669 **ChIP-seq data processing**

670   Reads were adaptor filtered, trimmed, mapped to mm9 using Bowtie2. From the mapped

671 reads duplicates and reads with a mapping quality below 20 were discarded. Quantification of

672 a region around the TSS which were defined in the previous section proceeded with the

673 following steps. Peaks in aligned reads for histone modifications were called using EPIC

674 (https://github.com/biocore-ntnu/epic), which is a more computationally efficient version of

675 SICER (*116*). Macs2 (*117*) was used to call peaks for the ATAC-seq data as no input sequencing

676 was done. Many of the histone modifications would vary substantially in terms of both the

677 number of reads in a set genomic region but also in terms of the width of the marked area. To

678 capture the variation in with the promoter modifications were quantified, for each of the

679 annotated transcriptional start sites (TSSs) with a window of 250 base pairs flanking the site

680 was quantified and extended to include overlapping peaks. All quantified promoter features

681 underwent a regularized log transform (*118*) and were scaled 0 to 1.

682   For RNAseq and H3K36me3 we altered our quantification strategy. H3K36me3 is a histone

683 modification associated with an elongating RNA polymerase II seem during active expression,

684 which is absent over the promoter. The H3K36me3 ChIP-seq was quantified across the entire

685 gene body and then divided by the length of the gene. The P7 RNAseq data was quantified

686 across all exons and divided by the total length of the exons. Both RNAseq and H3K36me3

687 were then scaled between 0 and 1.

688   To calculate the enrichment of chromatin modifications, epigenetic features were

689 separated based upon the distribution of the quantified modifications. The normalized data

690   show a clearly bimodal distribution or a distribution with a large upper tail. Marked or bound

691   versus unmarked or unbound genes could be distinguished by fitting two normal distributions.

692   First long upper tails were removed by calculating the first order derivative of the smoothed

693   ranked data similar to how super enhancers are identified (*42*). We set the threshold for the

694   long upper tails at 0.0004 pragmatically. The remainder of the datapoints for each tracks were

695   split using a mixture of Gaussian distributions using mixtools (*119*). Each data set were split

696   into marked/unmarked/tail for the enrichment calculation and for plotting.

697   **RNA-seq**

698   RNA was extracted using Trizol (Invitrogen), with and mechanical disruption with a 1.5 ul

699   tube mortise and pestle. Following precipitation, the RNA was treated with DNase1 and

700   cleaned up with a RNAeasy colomn (Qiagen). RNA was quantified with the Qubit and the

701   quality of the RNA was assayed using Agilent Bioanalyzer. Libraries were prepared using mRNA

702   purified using polyA bead selection (New England Biolabs), using Illumina TruSeq v2 library

703   preparation kit (Illumina). Sequencing was performed using HiSeq 2500 with 100 BP single-end

704   to approximately 60-70 million reads per sample.

705   **Generating cell type-specific transcript models**

706   Since we were attempting to identify epigenetic regulatory features by looking for common

707   signatures present in a large number of genes, it was important that each protein coding gene

708   would be counted roughly equally. Some genes have numerous annotated TSS while others

709   only have one and the discrepancy could bias the downstream analysis. We wanted to

710   represent each protein coding gene with at least one TSS and one transcript model but

711   permitted a gene to have multiple TSS and associated transcript models if there was evidence in

712   the ChIP-seq data of an additional TSS. We used both the Ensembl mouse 67 annotation

713   system as well as the UCSC mm9 knownGene annotation to generate a robust list of baseline

714   TSSs and transcript models. The TSS in the reference annotation was quantified using both the

715   GNP H3K4me3 data and the adult cerebellum H3K4me3 data from the Encode project (*120*).

716   For genes with clear H3K4me3 binding we selected transcripts with the strongest H3K4me3 at

717   the TSS or within 500 BP of the optimal TSS. For genes without clear H3K4me3 over any

718   transcript we took the maximum of all of the other modifications annotated over potential TSS.

719   To identify the best transcript model for each gene from the numerous in the reference

720   transcriptome we performed de-novo transcript assembly from 1 replicate in each of the time

721   points in the RNA-seq data using Stringtie (*121*). The time point transcript assemblies were

722   then merged using Stringtie merge without the reference annotation. Both selecting a TSS and

723   transcript model using only de novo assembly is complicated by a number of issues. The PolyA

724   selection is 3' biased, which will bias the de novo transcript models towards TSS which occur in

725   the 3' direction in a manner that is worse for low expressed genes. We calculated an overlap

726   for each transcript between the reference transcript library (UCSC and ensemble) and the

727   Stringtie models using Bedtools (*122*). We then selected a transcript model from the reference

728   with the highest overlap to the Stringtie models for each gene.

729   **RNAseq quantification**

730   The RNAseq data was mapped to mm9 using Tophat2 (*123*), so the last mm9 associated

731   Ensembl release (release 67) was used as reference transcriptome. The transcript models used

732   to quantify the RNAseq data developed as described above. Transcripts were quantified with

37

733   HTSEQ. The overall pipeline was developed with modification from the Bradner lab pipeline

734   (https://github.com/BradnerLab/pipeline).

735   **Processing existing data sets**

736   The Hatten lab NeuroD1-TRAP data was downloaded from GEO (GSE74400) and the

737   Affemetrix annotations linked to the Ensembl mouse 67 transcript models were downloaded

738   using biomaRt. Initial analysis was performed using oligo and limma packages from

739   Bioconductor. The probes were then collapsed to the transcript models described above.

740   The scRNAseq data from the Taylor lab was obtained from GEO (*31*) and the reads were

741   processed using the DropletUtils package from Bioconductor. We used the annotated cluster

742   to cell tables provided in the supplementary data to reconstruct the data. The granule neuron

743   lineages were separated from other cell types like Purkinje cells, astrocytes. In order to

744   eliminate genes from the bulk RNAseq that were likely arising from non-granule neuron lineage

745   we used the existing cell type clustering analysis done by the Taylor lab using Seurat.   The cell

746   types were separated into granule neuron lineage and non GN lineage. For each gene, across

747   the cell types, the highest expression in GN lineage and the non GN lineage cells was calculated.

748   By comparing the maximum GN expression to non GN expression we excluded genes with the

749   following 3 criteria. We excluded genes that were expressed in alternative lineages when not

750   expressed at all in the GN lineage cells, genes that were 2 fold higher in non GN or when they

751   were significantly higher expressed in non GN lineage by the Taylor lab Seurat analysis.

752

Differentiation gene classification

Expression cutoffs for transcriptional time course data were established using the distribution of the maximal values from the time course. For each dataset the average maximum of the 3 highest expressed timepoints/replicates were taken. Based upon the distribution we created a mixture model to estimate the point at which the probability of the expressed versus unexpressed distribution was equal to .50. For the Scott lab RNAseq dataset the count data was highly zero weighted, so we utilized a mixture of 2 gamma distributions (*124*). The Hatten lab TRAP data was modeled using 2 normal distributions. The transcriptional profiles were merged by interpolating the overlapping time points. We then calculated the timepoint that had the maximum and minimum RNA using the combined dataset. Using the maximum and minimum values we calculated a fold change using both datasets. We also estimated the developing time point at which the gene reached 50% of its maximum transcript abundance (t50). In order to be accepted as a significant changer p-values were calculated based upon each dataset individually, using DEseq2 (*118*) for the RNAseq dataset and limma (*125*) for the TRAP data.

Mouse husbandry

Ezh2 conditional knockout (Math1$^{Cre;}$ *Ezh2*$^{flox/flox}$) mice were generated by crossing Math1>Cre (*56*) with the *Ezh2*$^{flox/flox}$ mouse where Loxp sites flank the catalytic SET domain of Ezh2 (*55*). Mice were then bred homozygous for the flox Ezh2 allele, and Cre negative littermates were used for controls. Math1>GFP (*30*) mice were maintained as homozygous. Math1$^{Cre;}$ *Ezh2*$^{flox/flox}$;Math1>GFP mice All animal studies were approved by the Stanford APLAC review board protocol .

Spontaneous MB tumor formation

ChIPseq and RNAseq data was generated from spontaneous MBs that occurred in Ptch1$^{+/-}$ mice, with MB formation determined by following for neurologic decline.   Since the generation of MBs can have severe neurological affects, animals were monitored daily for physical abnormalities such as ataxia, hunching, immobility. Math1$^{Cre;}$ *Ezh2*$^{flox/flox}$;Ptch1$^{+/-}$ and *Ezh2*$^{flox/flox}$;Ptch1$^{+/-}$ mice were also generated to test the effect of *Ezh2* cKO on MB formation.

Table 2: Mice alleles used

Allele	RRID
Math1-Cre	IMSR_JAX:011104
Ezh2^{flox}	MMRRC_015499-UNC
Math1-GFP	MGI:4456122
Ptch1+/-	IMSR_JAX:003081

Edu pulse/chase

To assess migration of the GNPs out of the EGL we performed 48 h Edu pulse chase. A single IP injection (50mg/kg using a 5mg/mL stock diluted in PBS) was administered to p5 *Ezh2* cKO and wild-type mice.   After 48 h, brains were dissected and fixed in 4% PFA overnight then transferred into 30% sucrose for 24h. Fixed whole cerebellum were mounted in OCT and sectioned at 20µm. EdU staining was performed as per manufacturers instructions (Life

789 Technologies, Clik-iT Plus EdU Alexa Fluor 647 Imaging Kit, cat no. C10640). Following Edu

790 labeling, sections were blocked in 0.2% triton X-100 and 5% Donkey serum 1h at RT. Sections

791 were then stained with Rabbit anti-p27 as described in the tissue immunofluorescence section.

792 **GNP isolation and purification**

793 The GNP extraction and purification has been previously described (*1, 126*). In brief, the

794 mice were euthanized and the cerebella were dissected and minced. The cerebellar pieces

795 were incubated with 10 U/ml papain (Worthington, NJ, United States, LSOO3126) and 250 U/ml

796 DNase (Sigma, MO, United States, D4627) in HBSS (Stem Cell Technologies Canada Inc,

797 Vancouver, Canada, 37150) at 37 C for 30 min and the papain was halted using 8 mg/ml

798 Ovomucoid (Sigma, MO, United States, T2011) and 8 mg/ml bovine serum albumin (Sigma).

799 The pieces were then sequentially triturated in the presence of DNase to prevent clumping,

800 then passed through a 70uM nylon cell strainer (VWR, 21,008-952). GNPs were isolated using a

801 35%, 65% Percoll (Sigma, P4937) step gradient with centrifugation at 2500 rpm for 15 min.

802 **E15.5 GNP purification**

803 Because of the small cell number and the contamination of Sox2 + cells we utilized FACS to

804 purify the pre-Shh GNPs. Timed pregnant mothers homozygous for the *Math1*-GFP reporter

805 were sacrificed using cervical dislocation following deep anesthesia. The embryos were

806 harvested, and the rhombic lip and cerebellar anlage were dissected using micro-scissors and

807 jeweller forceps. The single cell suspension was generated as above. GFP+ were isolated using

808 standard FACS technique. The cells were then lyzed in Trizol without centrifugation and RNA

809 purification proceeded immediately.

MB cell culture

MB cell lines (*61*) generated from *Ptch1*$^{+/-}$ mice by the Seghal Lab (Dana-Farber Cancer

Institute, Harvard Medical School), and *Ptch1*$^{+/-}$; *Tpr53*$^{-/-}$ from the Rudin Lab (Memorial Sloan

Kettering Cancer Center), were grown as suspension as neurospheres. Briefly, cells were

maintained in DMEM/F12 supplemented with glutamine and with B27 minus vitamin A,

penicillin and streptomycin. The cells were passaged every 6 days by collecting the spheres by

gravity, washing, followed by dissociation with Accutase (Stemcell Technologies 07920) and

replating as a suspension to allow cells to spontaneously re-aggregate. UNC1999 was soluble in

DMSO while Palbociclib was soluble in water (Selleckchem).

GNP culture

P7 GNPs were purified as described above. The cerebella dissected either from the *Ezh2*

cKO described above or from mice with a Math1>GFP (*30*) reporter that delineates transit

amplifying GNPs from differentiated cells. The GNPs were grown as described previously for

our GNP proliferation conditions (*1*) with 3ng/ml of Shh 461-54 (R&D systems). The cells were

fixed at 24 h and immunofluorescence imaging occurred.   To measure the protein abundance

of the product from the differentiation genes, the freshly isolated cells were plated without Shh

to induce differentiation, fixed after 6h, 24h or 48h in culture.

Cell culture imaging

All cell culture imaging for both GNPs and MB cells was performed on 96 well, glass bottom

plates (Cellvis P96-1.5H-N). The plates were coated with 100 ug/ml PDL (Millipore A-003-E) for

3 h at 37 C, then washed, and coated with 10 ug/ml Lamnin (Millipore CC095) overnight at 37 C.

GNPs were purified as described above and MB cells were dissociated with Accutase as

832   described above, then filtered using a 70-micron to remove clusters of cells. Following cell

833   counting 10,000 cells were plated per well and perturbations were performed 2h after plating.

834   Following treatment, the cells were fixed with 4% paraformaldehyde for 10 min at room

835   temperature. The cells were then blocked using 5% donkey serum, 1% BSA and 0.2% triton X-

836   100 for 1h at room temperature. Primary antibodies were incubated overnight at 4 C. The

837   primary antibodies used are described in table 3. Cells were co-stained with Rhodamine

838   Phalloidin (Molecular Probes R415). Donkey anti IgG secondary antibodies against mouse and

839   rabbit were used conjugated to Alexa-488 and Alexa-647 at 1:500 (Jackson Immunoresearch).

840   All cell imaging was performed using the ImageXpress Micro XLS Widefield High Content

841   Screening System (Molecular Devices, Sunnyvale, CA) using 20x (0.75 NA) Nikon objectives. The

842   intensity of fluorescence in each cell was automatically calculated using custom MATLAB

843   scripts. Nuclei were segmented using DAPI as previously described (*127*). Downstream analysis

844   was performed in R.

845

846 *Table 3*: Antibodies used for immunofluorescence

Antibody	Vendor	Species	Serotype	Catalog	Dilution	RRID
NeuN	Millipore	mouse monoclonal	IgG	MAB377	1:200	AB_2298772
Phospho-Rb (Ser807/811) clone D20B12	Cell Signaling Technology	rabbit monoclonal	IgG	8516	1:1000	AB_11178658
p27	Abcam	Rabbit monoclonal	IgG	ab32034	1:100	AB_2244732
Cbx7	Abcam	Rabbit polyclonal	IgG	ab21873	1:200	AB_726005
H3K27me3	Active Motif	Rabbit polyclonal	IgG	39155	1:200	AB_2561020
Map2	Abcam	Chicken polyclonal	IgG	ab5392	1:2500	AB_2138153
Ezh2 clone D2C9	Cell Signaling Technology	Rabbit monoclonal	IgG	5246	1:200	AB_10694683

847 **Tissue Immunofluorescence**

848   P7 mice were perfused with 4% PFA, then fixed for 16 h. Fixed whole cerebellum were

849 mounted in OCT and sectioned at 20μm. Antigen retrieval was performed only for Cbx7 using

850 10 mM Citrate pH 6 buffer, boiled for 15 min.   Immunofluorescence proceeded as described in

851 the cell culture staining protocol.   Panoramic Imaging was done on a Zeiss Axioimager and 40x

852 confocal micrographs were generated using a Leica Sp2 confocal microscope.

853 **Cerebellar layer segmentation**

854   To segment the cerebellum into outer EGL, inner EGL, ML, IGL and deep white matter we

855 generated panoramic tiled immunofluorescence images of the P7 cerebellum, with DAPI, NeuN

856 (Alexa 488) and p27 (Alexa 647). The images were then background corrected and stitched in

857 Fiji (Image J) using Grid/Collection with 20% overlap. A custom MATLAB script was then used to

44

858 perform the segmentation. The first pass performed preprocessing on the image and coarsely

859 identified each layer using a combination or ratio of the individual channels. The IGL was

860 defined as NeuN high, the inner EGL as p27 high, and the outer EGL as DAPI high. Each layer of

861 the cerebellum borders the following layer, allowing previously established layers to serve as

862 guides for the development of following layers. Beginning from the inner most layer, through

863 to the outermost, dilations were used to define and fill out the regions of interest. The pixels of

864 each region were filtered and smoothed to promote clear boundaries between the layers. A

865 composite image was then produced containing all the regions. With each region clearly

866 defined, calculations for segmented pixel area and region measurements for NeuN, P27, and

867 DAPI fluorescence intensity for each layer could be determined.

868 **Cerebellar immunofluorescence quantification**

869 The images were generated as described above. Linear segments centered along the pia,

870 with an EGL on either side were selected and made into separate images. The image segments

871 were further subdivided into 200 pixel sections moving perpendicular to the axis of the EGL. A

872 line track was generated by taking the pixel mean perpendicular to the EGL. The individual line

873 segments were then aligned using cross-correlation from the Stats package in R. After

874 alignment the symmetric line segment was split by calculating the local minimum near the

875 center of the dataset for an average p27 intensity of the entire dataset. The center was set to 0

876 on the x-axis which allowed us to split each line segment into 2 moving from 0 the pial

877 boundary to the IGL at the highest values. There was variability in the distance from the center

878 point to the pial boundary where the EGL starts caused by a gap in the arachnoid along the

879 invagination of the folia. The pial boundary was determined as a drop off in the

880   immunofluorescence background. To find this boundary we identified the peak change in the

881   product of NeuN and p27 values.

882   **Quantification of cell cycle and differentiation and process extension**

883   Dead cells and G2 cells were separated from G0/1 cells using the cell pixel area and DAPI

884   median values, then G0, G1 and G2 were further separated according to the level of Ki67 or RB

885   phosphorylation (Ser807/811). Differentiated cells were identified using a cut-off value for

886   NeuN immunofluorescence only accepting differentiating cells if they are marked as G0 by the

887   above-described criteria. Process extension and process length was quantified using

888   Neuroncyto 2 (*60*) image by image using Map2 immunofluorescence with DAPI labeling of the

889   nuclei.

890

891

Additional information

Data availability and resource sharing

Data supporting this study are available in GEO GSE279346 and GSE279347. Custom

analysis scripts are available following GITHUB repositories; jpurzner/seq_pipelines,

jpurzner/chip_tools, jpurzner/cell_culture_segment, jpurzner/layer_quant,

jpurzner/cerebellar_segmentation.

Author contributions

JP, ASB, TP, KW, MDT, YJT, MTF, MPS designed research. JP, ASB, TP, LE, SB, UL, AK, KW

performed research. JP, ASB, TP, KA, AS, KW, MDT, YJT, MTF, MPS analyzed data. JP, TP, ASB

and MPS wrote the paper.

Conflicts of interest

The authors declare no conflicts of interest.

References

1. R. J. Wechsler-Reya, M. P. Scott, Control of neuronal precursor proliferation in the cerebellum by Sonic Hedgehog. *Neuron* **22**, 103-114 (1999).

2. P. M. Lewis, A. Gritli-Linde, R. Smeyne, A. Kottmann, A. P. McMahon, Sonic hedgehog signaling is required for expansion of granule neuron precursors and patterning of the mouse cerebellum. *Dev Biol* **270**, 393-410 (2004).

3. V. A. Wallace, Purkinje-cell-derived Sonic hedgehog regulates granule neuron precursor cell proliferation in the developing mouse cerebellum. *Current biology : CB* **9**, 445-448 (1999).

4. A. M. Kenney, M. D. Cole, D. H. Rowitch, Nmyc upregulation by sonic hedgehog signaling promotes proliferation in developing cerebellar granule neuron precursors. *Development* **130**, 15-28 (2003).

5. A. M. Kenney, D. H. Rowitch, Sonic hedgehog promotes G(1) cyclin expression and sustained cell cycle progression in mammalian neuronal precursors. *Mol Cell Biol* **20**, 9055-9067 (2000).

6. Z. J. Yang *et al.*, Medulloblastoma can be initiated by deletion of Patched in lineage-restricted progenitors or stem cells. *Cancer cell* **14**, 135-145 (2008).

7. V. Ramaswamy, C. Nor, M. D. Taylor, p53 and Meduloblastoma. *Cold Spring Harbor perspectives in medicine* **6**, (2015).

8. N. Zhukova *et al.*, Subgroup-specific prognostic implications of TP53 mutation in medulloblastoma. *Journal of clinical oncology : official journal of the American Society of Clinical Oncology* **31**, 2927-2935 (2013).

9. F. M. G. Cavalli *et al.*, Intertumoral Heterogeneity within Medulloblastoma Subgroups. *Cancer cell* **31**, 737-754 e736 (2017).

10. M. Kool *et al.*, Genome sequencing of SHH medulloblastoma predicts genotype-related response to smoothened inhibition. *Cancer cell* **25**, 393-405 (2014).

11. D. J. Mabbott, L. Penkman, A. Witol, D. Strother, E. Bouffet, Core neurocognitive functions in children treated for posterior fossa tumors. *Neuropsychology* **22**, 159-168 (2008).

12. D. J. Mabbott *et al.*, Serial evaluation of academic and behavioral outcome after treatment with cranial radiation in childhood. *Journal of clinical oncology : official journal of the American Society of Clinical Oncology* **23**, 2256-2263 (2005).

13. L. Dirven *et al.*, Neurocognitive functioning and health-related quality of life in adult medulloblastoma patients: long-term outcomes of the NOA-07 study. *Journal of neuro-oncology* **148**, 117-130 (2020).

14. C. G. Eberhart, W. E. Kaufman, T. Tihan, P. C. Burger, Apoptosis, neuronal maturation, and neurotrophin expression within medulloblastoma nodules. *Journal of neuropathology and experimental neurology* **60**, 462-469 (2001).

15. P. C. Burger, F. C. Grahmann, A. Bliestle, P. Kleihues, Differentiation in the medulloblastoma. A histological and immunohistochemical study. *Acta neuropathologica* **73**, 115-123 (1987).

949 16. R. T. Meurer *et al.*, Immunohistochemical expression of markers Ki-67, neun,
950 synaptophysin, p53 and HER2 in medulloblastoma and its correlation with
951 clinicopathological parameters. *Arquivos de neuro-psiquiatria* **66**, 385-390 (2008).

952 17. H. Zhao, O. Ayrault, F. Zindy, J. H. Kim, M. F. Roussel, Post-transcriptional down-
953 regulation of Atoh1/Math1 by bone morphogenic proteins suppresses medulloblastoma
954 development. *Genes Dev* **22**, 722-727 (2008).

955 18. I. Rios, R. Alvarez-Rodriguez, E. Marti, S. Pons, Bmp2 antagonizes sonic hedgehog-
956 mediated proliferation of cerebellar granule neurones through Smad5 signalling.
957 *Development* **131**, 3159-3168 (2004).

958 19. J. S. Espinosa, L. Luo, Timing neurogenesis and differentiation: insights from quantitative
959 clonal analyses of cerebellar granule cells. *J Neurosci* **28**, 2301-2312 (2008).

960 20. T. Kim, H. Park, K. Tanaka-Yamamoto, Y. Yamamoto, Developmental timing-dependent
961 organization of synaptic connections between mossy fibers and granule cells in the
962 cerebellum. *Commun Biol* **6**, 446 (2023).

963 21. J. K. Rhee, H. Park, T. Kim, Y. Yamamoto, K. Tanaka-Yamamoto, Projection-dependent
964 heterogeneity of cerebellar granule cell calcium responses. *Molecular brain* **14**, 63
965 (2021).

966 22. S. A. Shuster *et al.*, The relationship between birth timing, circuit wiring, and
967 physiological response properties of cerebellar granule cells. *Proc Natl Acad Sci U S A*
968 **118**, (2021).

969 23. K. Leto *et al.*, Consensus Paper: Cerebellar Development. *Cerebellum*, (2015).

970 24. A. Chedotal, Should I stay or should I go? Becoming a granule cell. *Trends Neurosci* **33**,
971 163-172 (2010).

972 25. X. Zhu *et al.*, Role of Tet1/3 Genes and Chromatin Remodeling Genes in Cerebellar
973 Circuit Formation. *Neuron* **89**, 100-112 (2016).

974 26. P. Skowron *et al.*, The transcriptional landscape of Shh medulloblastoma. *Nature*
975 *communications* **12**, 1749 (2021).

976 27. A. Shearn, G. Hersperger, E. Hersperger, Genetic analysis of two allelic temperature-
977 sensitive mutants of Drosophila melanogaster both of which are zygotic and maternal-
978 effect lethals. *Genetics* **89**, 341-353 (1978).

979 28. E. A. Carrington, R. S. Jones, The Drosophila Enhancer of zeste gene encodes a
980 chromosomal protein: examination of wild-type and mutant protein distribution.
981 *Development* **122**, 4073-4083 (1996).

982 29. D. C. Tkachuk, S. Kohler, M. L. Cleary, Involvement of a homolog of Drosophila trithorax
983 by 11q23 chromosomal translocations in acute leukemias. *Cell* **71**, 691-700 (1992).

984 30. E. A. Lumpkin *et al.*, Math1-driven GFP expression in the developing nervous system of
985 transgenic mice. *Gene expression patterns : GEP* **3**, 389-395 (2003).

986 31. M. C. Vladoiu *et al.*, Childhood cerebellar tumours mirror conserved fetal transcriptional
987 programs. *Nature* **572**, 67-73 (2019).

988 32. R. Machold, C. Klein, G. Fishell, Genes expressed in Atoh1 neuronal lineages arising from
989 the r1/isthmus rhombic lip. *Gene expression patterns : GEP* **11**, 349-359 (2011).

990 33. D. Morales, M. E. Hatten, Molecular markers of neuronal progenitors in the embryonic
991 cerebellar anlage. *J Neurosci* **26**, 12226-12236 (2006).

34. R. Cao *et al.*, Role of histone H3 lysine 27 methylation in polycomb-group silencing. *Science* **298**, 1039-1043 (2002).

35. H. B. Wang *et al.*, Role of histone H2A ubiquitination in polycomb silencing. *Nature* **431**, 873-878 (2004).

36. T. Rauch, G. P. Pfeifer, Methylated-CpG island recovery assay: a new technique for the rapid detection of methylated-CpG islands in cancer. *Laboratory investigation; a journal of technical methods and pathology* **85**, 1172-1180 (2005).

37. M. P. Creyghton *et al.*, Histone H3K27ac separates active from poised enhancers and predicts developmental state. *Proc Natl Acad Sci U S A* **107**, 21931-21936 (2010).

38. A. Rada-Iglesias *et al.*, A unique chromatin signature uncovers early developmental enhancers in humans. *Nature* **470**, 279-283 (2011).

39. N. D. Heintzman *et al.*, Histone modifications at human enhancers reflect global cell-type-specific gene expression. *Nature* **459**, 108-112 (2009).

40. N. D. Heintzman *et al.*, Distinct and predictive chromatin signatures of transcriptional promoters and enhancers in the human genome. *Nat Genet* **39**, 311-318 (2007).

41. J. D. Buenrostro, B. Wu, H. Y. Chang, W. J. Greenleaf, ATAC-seq: A Method for Assaying Chromatin Accessibility Genome-Wide. *Curr Protoc Mol Biol* **109**, 21 29 21-29 (2015).

42. W. A. Whyte *et al.*, Master transcription factors and mediator establish super-enhancers at key cell identity genes. *Cell* **153**, 307-319 (2013).

43. R. Margueron, D. Reinberg, The Polycomb complex PRC2 and its mark in life. *Nature* **469**, 343-349 (2011).

44. A. Hugues, C. S. Jacobs, F. Roudier, Mitotic Inheritance of PRC2-Mediated Silencing: Mechanistic Insights and Developmental Perspectives. *Frontiers in plant science* **11**, 262 (2020).

45. U. Jadhav *et al.*, Replicational Dilution of H3K27me3 in Mammalian Cells and the Role of Poised Promoters. *Mol Cell* **78**, 141-151 e145 (2020).

46. R. T. Coleman, G. Struhl, Causal role for inheritance of H3K27me3 in maintaining the OFF state of a Drosophila HOX gene. *Science* **356**, (2017).

47. P. Asp *et al.*, Genome-wide remodeling of the epigenetic landscape during myogenic differentiation. *Proc Natl Acad Sci U S A* **108**, E149-158 (2011).

48. D. S. Gilmour, J. T. Lis, RNA polymerase II interacts with the promoter region of the noninduced hsp70 gene in Drosophila melanogaster cells. *Mol Cell Biol* **6**, 3984-3989 (1986).

49. D. J. Huebert, M. Kamal, A. O'Donovan, B. E. Bernstein, Genome-wide analysis of histone modifications by ChIP-on-chip. *Methods* **40**, 365-369 (2006).

50. T. S. Mikkelsen *et al.*, Genome-wide maps of chromatin state in pluripotent and lineage-committed cells. *Nature* **448**, 553-560 (2007).

51. N. P. Blackledge *et al.*, Variant PRC1 complex-dependent H2A ubiquitylation drives PRC2 recruitment and polycomb domain formation. *Cell* **157**, 1445-1459 (2014).

52. M. Ku *et al.*, Genomewide analysis of PRC1 and PRC2 occupancy identifies two classes of bivalent domains. *PLoS Genet* **4**, e1000242 (2008).

53. E. Vire *et al.*, The Polycomb group protein EZH2 directly controls DNA methylation. *Nature* **439**, 871-874 (2006).

54. D. O'Carroll *et al.*, The polycomb-group gene Ezh2 is required for early mouse development. *Mol Cell Biol* **21**, 4330-4336 (2001).

55. I. H. Su *et al.*, Ezh2 controls B cell development through histone H3 methylation and Igh rearrangement. *Nat Immunol* **4**, 124-131 (2003).

56. V. Matei *et al.*, Smaller inner ear sensory epithelia in Neurog 1 null mice are related to earlier hair cell cycle exit. *Dev Dyn* **234**, 633-650 (2005).

57. J. Muller *et al.*, Histone methyltransferase activity of a Drosophila Polycomb group repressor complex. *Cell* **111**, 197-208 (2002).

58. S. Erhardt *et al.*, Consequences of the depletion of zygotic and embryonic enhancer of zeste 2 during preimplantation mouse development. *Development* **130**, 4235-4248 (2003).

59. R. Margueron *et al.*, Ezh1 and Ezh2 maintain repressive chromatin through different mechanisms. *Mol Cell* **32**, 503-518 (2008).

60. K. H. Ong, J. De, L. Cheng, S. Ahmed, W. Yu, NeuronCyto II: An automatic and quantitative solution for crossover neural cells in high throughput screening. *Cytometry. Part A : the journal of the International Society for Analytical Cytology* **89**, 747-754 (2016).

61. X. Zhao *et al.*, RAS/MAPK Activation Drives Resistance to Smo Inhibition, Metastasis, and Tumor Evolution in Shh Pathway-Dependent Tumors. *Cancer research* **75**, 3623-3635 (2015).

62. K. D. Konze *et al.*, An orally bioavailable chemical probe of the Lysine Methyltransferases EZH2 and EZH1. *ACS chemical biology* **8**, 1324-1334 (2013).

63. D. W. Fry *et al.*, Specific inhibition of cyclin-dependent kinase 4/6 by PD 0332991 and associated antitumor activity in human tumor xenografts. *Molecular cancer therapeutics* **3**, 1427-1438 (2004).

64. L. V. Goodrich, L. Milenkovic, K. M. Higgins, M. P. Scott, Altered neural cell fates and medulloblastoma in mouse patched mutants. *Science* **277**, 1109-1113 (1997).

65. T. G. Oliver *et al.*, Loss of patched and disruption of granule cell development in a pre-neoplastic stage of medulloblastoma. *Development* **132**, 2425-2439 (2005).

66. T. Purzner *et al.*, Developmental phosphoproteomics identifies the kinase CK2 as a driver of Hedgehog signaling and a therapeutic target in medulloblastoma. *Sci Signal* **11**, (2018).

67. K. Matlik, E. E. Govek, M. R. Paul, C. D. Allis, M. E. Hatten, Histone bivalency regulates the timing of cerebellar granule cell development. *Genes Dev* **37**, 570-589 (2023).

68. V. Ramesh, F. Liu, M. S. Minto, U. Chan, A. E. West, Bidirectional regulation of postmitotic H3K27me3 distributions underlie cerebellar granule neuron maturation dynamics. *eLife* **12**, (2023).

69. X. Feng *et al.*, Polycomb Ezh2 controls the fate of GABAergic neurons in the embryonic cerebellum. *Development* **143**, 1971-1980 (2016).

70. C. Mozzetta *et al.*, Selective control of Pax7 expression by TNF-activated p38alpha/polycomb repressive complex 2 (PRC2) signaling during muscle satellite cell differentiation. *Cell Cycle* **10**, 191-198 (2011).

1077 71. A. H. Juan *et al.*, Polycomb EZH2 controls self-renewal and safeguards the transcriptional
1078   identity of skeletal muscle stem cells. *Genes Dev* **25**, 789-794 (2011).
1079 72. G. Caretti, M. Di Padova, B. Micales, G. E. Lyons, V. Sartorelli, The Polycomb Ezh2
1080   methyltransferase regulates muscle gene expression and skeletal muscle differentiation.
1081   *Genes Dev* **18**, 2627-2638 (2004).
1082 73. A. He *et al.*, Polycomb repressive complex 2 regulates normal development of the
1083   mouse heart. *Circulation research* **110**, 406-415 (2012).
1084 74. X. P. Yang *et al.*, EZH2 is crucial for both differentiation of regulatory T cells and T
1085   effector cell expansion. *Scientific reports* **5**, 10643 (2015).
1086 75. B. P. Coe *et al.*, Genomic deregulation of the E2F/Rb pathway leads to activation of the
1087   oncogene EZH2 in small cell lung cancer. *PLoS One* **8**, e71670 (2013).
1088 76. A. P. Bracken *et al.*, EZH2 is downstream of the pRB-E2F pathway, essential for
1089   proliferation and amplified in cancer. *Embo J* **22**, 5323-5335 (2003).
1090 77. R. Wijayatunge *et al.*, The histone demethylase Kdm6b regulates a mature gene
1091   expression program in differentiating cerebellar granule neurons. *Mol Cell Neurosci* **87**,
1092   4-17 (2018).
1093 78. A. H. Cleveland *et al.*, PRC2 disruption in cerebellar progenitors produces cerebellar
1094   hypoplasia and aberrant myoid differentiation without blocking medulloblastoma
1095   growth. *Acta neuropathologica communications* **11**, 8 (2023).
1096 79. K. Jun *et al.*, Ablation of P/Q-type Ca(2+) channel currents, altered synaptic
1097   transmission, and progressive ataxia in mice lacking the alpha(1A)-subunit. *Proc Natl
1098   Acad Sci U S A* **96**, 15245-15250 (1999).
1099 80. H. Komuro, P. Rakic, Modulation of neuronal migration by NMDA receptors. *Science* **260**,
1100   95-97 (1993).
1101 81. M. Farrant, D. Feldmeyer, T. Takahashi, S. G. Cull-Candy, NMDA-receptor channel
1102   diversity in the developing cerebellum. *Nature* **368**, 335-339 (1994).
1103 82. D. J. Rossi, N. T. Slater, The developmental onset of NMDA receptor-channel activity
1104   during neuronal migration. *Neuropharmacology* **32**, 1239-1248 (1993).
1105 83. C. Akazawa, R. Shigemoto, Y. Bessho, S. Nakanishi, N. Mizuno, Differential expression of
1106   five N-methyl-D-aspartate receptor subunit mRNAs in the cerebellum of developing and
1107   adult rats. *The Journal of comparative neurology* **347**, 150-160 (1994).
1108 84. M. Watanabe, M. Mishina, Y. Inoue, Distinct spatiotemporal expressions of five NMDA
1109   receptor channel subunit mRNAs in the cerebellum. *The Journal of comparative
1110   neurology* **343**, 513-519 (1994).
1111 85. K. Tarnok, K. Czondor, M. Jelitai, A. Czirok, K. Schlett, NMDA receptor NR2B subunit
1112   over-expression increases cerebellar granule cell migratory activity. *Journal of
1113   neurochemistry* **104**, 818-829 (2008).
1114 86. K. Schlett *et al.*, Long-term NR2B expression in the cerebellum alters granule cell
1115   development and leads to NR2A down-regulation and motor deficits. *Mol Cell Neurosci*
1116   **27**, 215-226 (2004).
1117 87. H. Komuro, P. Rakic, Selective role of N-type calcium channels in neuronal migration.
1118   *Science* **257**, 806-809 (1992).

1119 88. P. Zhou *et al.*, Polarized signaling endosomes coordinate BDNF-induced chemotaxis of
1120 cerebellar precursors. *Neuron* **55**, 53-68 (2007).
1121 89. P. R. Borghesani *et al.*, BDNF stimulates migration of cerebellar granule cells.
1122 *Development* **129**, 1435-1442 (2002).
1123 90. M. Kokubo *et al.*, BDNF-mediated cerebellar granule cell development is impaired in
1124 mice null for CaMKK2 or CaMKIV. *J Neurosci* **29**, 8901-8913 (2009).
1125 91. S. Pons, J. L. Trejo, J. R. Martinez-Morales, E. Marti, Vitronectin regulates Sonic
1126 hedgehog activity during cerebellum development through CREB phosphorylation.
1127 *Development* **128**, 1481-1492 (2001).
1128 92. G. U. Hoglinger *et al.*, The pRb/E2F cell-cycle pathway mediates cell death in Parkinson's
1129 disease. *Proc Natl Acad Sci U S A* **104**, 3585-3590 (2007).
1130 93. K. L. Jordan-Sciutto, L. M. Malaiyandi, R. Bowser, Altered distribution of cell cycle
1131 transcriptional regulators during Alzheimer disease. *Journal of neuropathology and*
1132 *experimental neurology* **61**, 358-367 (2002).
1133 94. H. Osuga *et al.*, Cyclin-dependent kinases as a therapeutic target for stroke. *Proc Natl*
1134 *Acad Sci U S A* **97**, 10254-10259 (2000).
1135 95. G. C. Wong, K. H. Chow, DNA Damage Response-Associated Cell Cycle Re-Entry and
1136 Neuronal Senescence in Brain Aging and Alzheimer's Disease. *J Alzheimers Dis* **94**, S429-
1137 S451 (2023).
1138 96. I. Blumcke, O. D. Wiestler, Gangliogliomas: an intriguing tumor entity associated with
1139 focal epilepsies. *Journal of neuropathology and experimental neurology* **61**, 575-584
1140 (2002).
1141 97. M. J. Hicks, B. Mackay, Comparison of ultrastructural features among neuroblastic
1142 tumors: maturation from neuroblastoma to ganglioneuroma. *Ultrastructural pathology*
1143 **19**, 311-322 (1995).
1144 98. E. Miele *et al.*, The histone methyltransferase EZH2 as a druggable target in SHH
1145 medulloblastoma cancer stem cells. *Oncotarget* **8**, 68557-68570 (2017).
1146 99. I. Alimova *et al.*, Targeting the enhancer of zeste homologue 2 in medulloblastoma.
1147 *International journal of cancer. Journal international du cancer* **131**, 1800-1809 (2012).
1148 100. Y. Cheng *et al.*, NeuroD1 Dictates Tumor Cell Differentiation in Medulloblastoma. *Cell*
1149 *reports* **31**, 107782 (2020).
1150 101. M. Leszczyniecka, T. Roberts, P. Dent, S. Grant, P. B. Fisher, Differentiation therapy of
1151 human cancer: basic science and clinical applications. *Pharmacology & therapeutics* **90**,
1152 105-156 (2001).
1153 102. G. B. Pierce, C. Wallace, Differentiation of malignant to benign cells. *Cancer research* **31**,
1154 127-134 (1971).
1155 103. G. B. Pierce, The cancer cell and its control by the embryo. Rous-Whipple Award lecture.
1156 *The American journal of pathology* **113**, 117-124 (1983).
1157 104. D. Head *et al.*, Effect of aggressive daunomycin therapy on survival in acute
1158 promyelocytic leukemia. *Blood* **86**, 1717-1728 (1995).
1159 105. H. J. Iland *et al.*, All-trans-retinoic acid, idarubicin, and IV arsenic trioxide as initial
1160 therapy in acute promyelocytic leukemia (APML4). *Blood* **120**, 1570-1580; quiz 1752
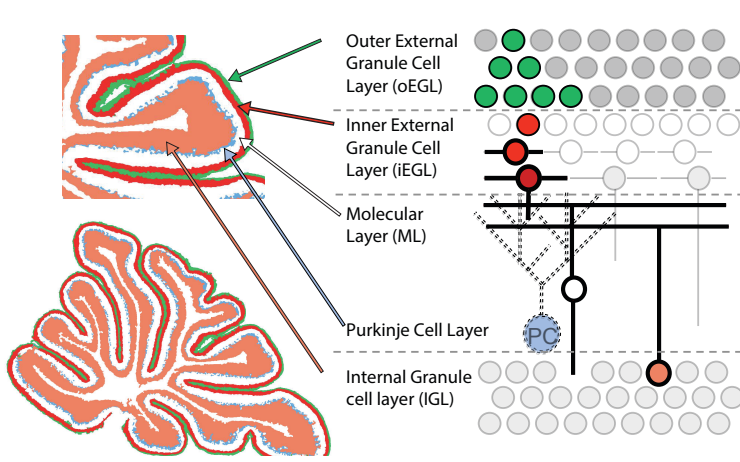1161 (2012).

106. F. Lo-Coco, L. Cicconi, M. Breccia, Current standard treatment of adult acute promyelocytic leukaemia. *British journal of haematology* **172**, 841-854 (2016).

107. Z. Y. Wang, Z. Chen, Acute promyelocytic leukemia: from highly fatal to highly curable. *Blood* **111**, 2505-2515 (2008).

108. Q. Chang *et al.*, All-trans-retinoic acid induces cell growth arrest in a human medulloblastoma cell line. *Journal of neuro-oncology* **84**, 263-267 (2007).

109. J. Liu, L. Guo, Y. Luo, J. W. Li, H. Li, All trans-retinoic acid suppresses in vitro growth and down-regulates LIF gene expression as well as telomerase activity of human medulloblastoma cells. *Anticancer research* **20**, 2659-2664 (2000).

110. A. R. Hallahan *et al.*, BMP-2 mediates retinoid-induced apoptosis in medulloblastoma cells through a paracrine effect. *Nature medicine* **9**, 1033-1038 (2003).

111. S. E. Spiller, S. H. Ditzler, B. J. Pullar, J. M. Olson, Response of preclinical medulloblastoma models to combination therapy with 13-cis retinoic acid and suberoylanilide hydroxamic acid (SAHA). *Journal of neuro-oncology* **87**, 133-141 (2008).

112. M. L. Cook Sangar *et al.*, Inhibition of CDK4/6 by Palbociclib Significantly Extends Survival in Medulloblastoma Patient-Derived Xenograft Mouse Models. *Clinical cancer research : an official journal of the American Association for Cancer Research* **23**, 5802-5813 (2017).

113. D. Van Mater *et al.*, A phase I trial of the CDK 4/6 inhibitor palbociclib in pediatric patients with progressive brain tumors: A Pediatric Brain Tumor Consortium study (PBTC-042). *Pediatric blood & cancer* **68**, e28879 (2021).

114. V. Dieras *et al.*, Long-term Pooled Safety Analysis of Palbociclib in Combination With Endocrine Therapy for HR+/HER2- Advanced Breast Cancer. *Journal of the National Cancer Institute* **111**, 419-430 (2019).

115. S. A. Blythe, C. D. Reid, D. S. Kessler, P. S. Klein, Chromatin immunoprecipitation in early Xenopus laevis embryos. *Dev Dyn* **238**, 1422-1432 (2009).

116. S. Xu, S. Grullon, K. Ge, W. Peng, Spatial clustering for identification of ChIP-enriched regions (SICER) to map regions of histone methylation patterns in embryonic stem cells. *Methods in molecular biology* **1150**, 97-111 (2014).

117. J. Feng, T. Liu, Y. Zhang, Using MACS to identify peaks from ChIP-Seq data. *Current protocols in bioinformatics / editoral board, Andreas D. Baxevanis ... [et al.]* **Chapter 2**, Unit 2 14 (2011).

118. M. I. Love, W. Huber, S. Anders, Moderated estimation of fold change and dispersion for RNA-seq data with DESeq2. *Genome Biol* **15**, 550 (2014).

119. T. Benaglia, D. Chauveau, D. R. Hunter, D. S. Young, mixtools: An R Package for Analyzing Mixture Models. *Journal of Statistical Software* **32**, 1 - 29 (2009).

120. F. Yue *et al.*, A comparative encyclopedia of DNA elements in the mouse genome. *Nature* **515**, 355-364 (2014).

121. M. Pertea *et al.*, StringTie enables improved reconstruction of a transcriptome from RNA-seq reads. *Nature biotechnology* **33**, 290-295 (2015).

122. A. R. Quinlan, I. M. Hall, BEDTools: a flexible suite of utilities for comparing genomic features. *Bioinformatics* **26**, 841-842 (2010).

1204   123.   C. Trapnell, L. Pachter, S. L. Salzberg, TopHat: discovering splice junctions with RNA-Seq.
1205   *Bioinformatics* **25**, 1105-1111 (2009).
1206   124.   L. Scrucca, M. Fop, T. B. Murphy, A. E. Raftery, mclust 5: Clustering, Classification and
1207   Density Estimation Using Gaussian Finite Mixture Models. *R J* **8**, 289-317 (2016).
1208   125.   I. Diboun, L. Wernisch, C. A. Orengo, M. Koltzenburg, Microarray analysis after RNA
1209   amplification can detect pronounced differences in gene expression using limma. *BMC*
1210   *genomics* **7**, 252 (2006).
1211   126.   H. Y. Lee, L. A. Greene, C. A. Mason, M. C. Manzini, Isolation and culture of post-natal
1212   mouse cerebellar granule neuron progenitor cells and neurons. *Journal of visualized*
1213   *experiments : JoVE*, (2009).
1214   127.   S. D. Cappell, M. Chung, A. Jaimovich, S. L. Spencer, T. Meyer, Irreversible APC(Cdh1)
1215   Inactivation Underlies the Point of No Return for Cell-Cycle Entry. *Cell* **166**, 167-180
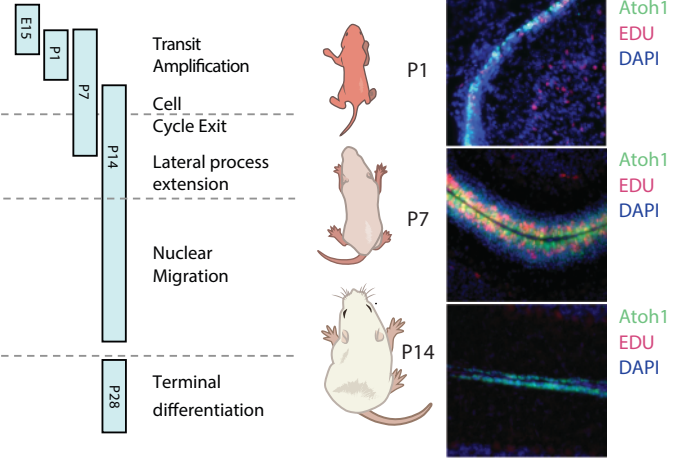1216   (2016).

1217

1218

Figure 1

A) Spatial Distribution of Stages in Cerebellar Development (P7)

Outer External Granule Cell Layer (oEGL)

Inner External Granule Cell Layer (iEGL)

Molecular Layer (ML)

Purkinje Cell Layer

PC

Internal Granule cell layer (IGL)

B) Temporal Distribution of Stages in Cerebellar Development

E15
P1
P7
P14
P28

Transit Amplification
Cell Cycle Exit
Lateral process extension
Nuclear Migration
Terminal differentiation

P1 — Atoh1 EDU DAPI

P7 — Atoh1 EDU DAPI

P14 — Atoh1 EDU DAPI

C)

Expressed n=15575

Granule neuron lineages n=12704

Dynamically expressed n=7334

Cell cycle n=997

Alternative lineage n=1874

Unexpressed n=4987

unchanged n=5370

excluded n=7858

excluded n=4987

P14 to P56 n=2675

P0 to P7 n=1750

E15 n=2784

incompatible max-min n=125

unchanged n=5370

excluded n=7858

P14 to P56 n=2050

P0 to P7 n=1434

E15 n=2294

p-val inadequate n=1431

unchanged n=5370

excluded n=7983

P14 to P56 n=1877

P0 to P7 n=1434

E15 n=2294

increase before P0 n=173

unchanged n=6801

excluded n=7983

>2 log2FC n=787
1-2 log2FC n=1090
>2 log2FC n=440
1-2 log2FC n=994
>2 log2FC n=783
1-2 log2FC n=1511

excluded n=14957

differentiation genes n=787
proliferation genes n=440
embryonic genes n=783

Final groups

Step 1: Remove unexpressed genes

Step 2: Remove genes contaminated from other lineages

Step 3: Remove genes that change < 2 fold

Step 4: Split genes based on time of max and min expression

Step 5: Remove genes p-val > 0.001 in differential expression

Step 6: Remove differentiation genes that increase most prior to P0

Step 7: Seperate by fold change

Figure 1: Identifying a high confidence group of genes that increase with GNP differentiation.

A) Schematic representation of the spatial distribution of stages of GNP development represented in the P7 mouse cerebellum. B) Schematic representation of the temporal distribution of the stages of GNP development. Stages represented in the RNASeq data are indicated by vertical bars. Representative sagittal slices of the cerebellum from mice harboring a *Math1-GFP* reporter, injected with EDU (1.5 h, red) and DAPI (blue) at P1, P7, and P14. **C**) A Sankey diagram describes how genes are partitioned in order to identify high confidence differentiation genes.   Briefly, genes are segregated by the following steps: 1, excluded genes by non-expression; 2, excluded genes by contamination from non granule neuron lineage identified through scRNAseq; 3, excluded by minimal change in expression during development; 4, segregated genes by the time of minimum and maximum expression (highest P14 to P6 differentiation genes, highest P0-7 proliferation genes, highest at E15 embryonic genes); 5 excluded genes by low statistical confidence; 6, exclude genes that increase prior to P0; 7, separate by fold-change (>2 fold log2 fold change or 1-2 log2 fold change) .
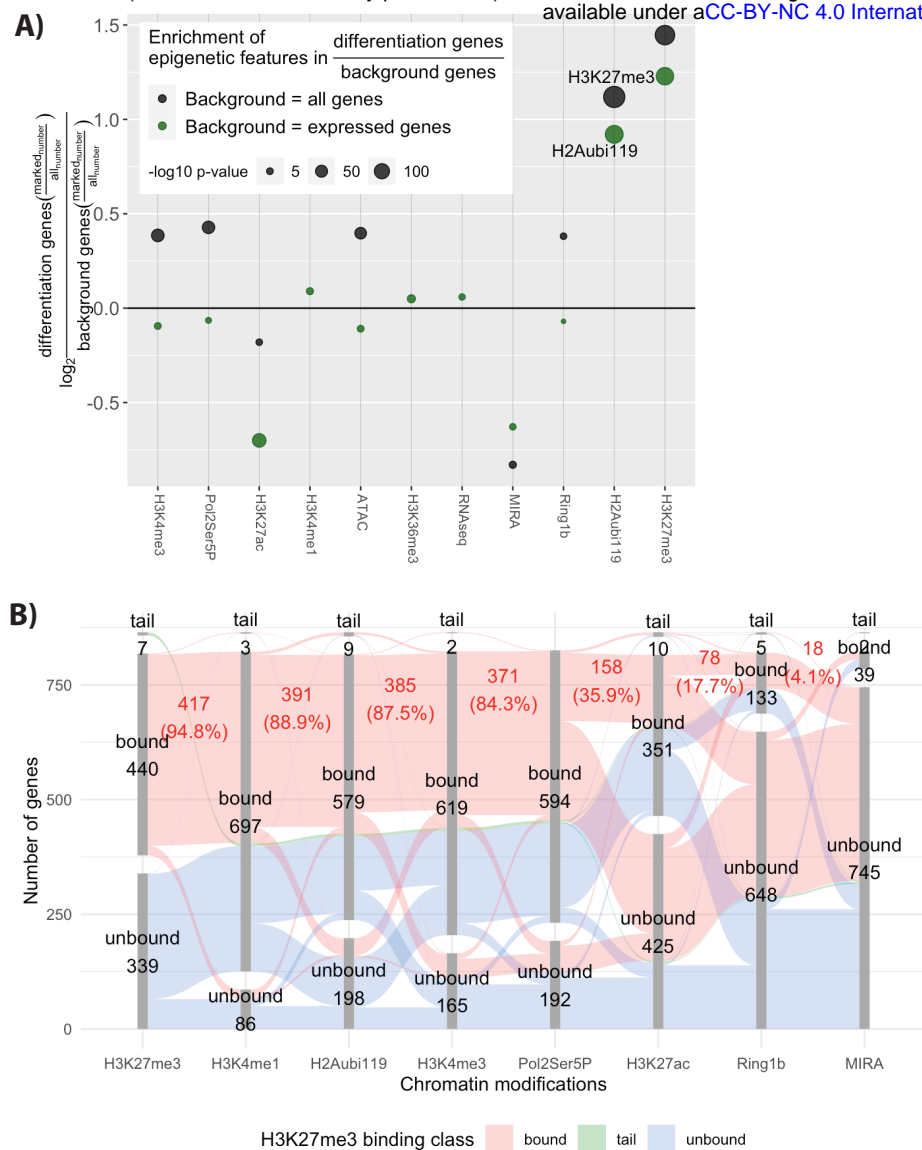
Figure 2: **H3K27me3 modification near the promoter of genes at P7 is associated with genes that increase later with differentiation.**

A) Enrichment of chromatin features near promoters of proliferating P7 GNP whose expression increases during differentiation. Enrichment is calculated for a given modification as the number of differentiation genes over either all genes (black) or genes expressed at any point during the granule neuron lineage (green). The log2 value of this fraction is then shown on the figure. The p-value is calculated using the hypergeometric test and the p-values are shown as the size of the dot. **B)** A parallel sets diagram that shows correlation between H3K27me3 binding and other modification. The disconnected bar graphs shows the number of genes that are bound or within the long upper tail for each modification. The red colour that spans the bar segments shows the genes that contain the next modification.
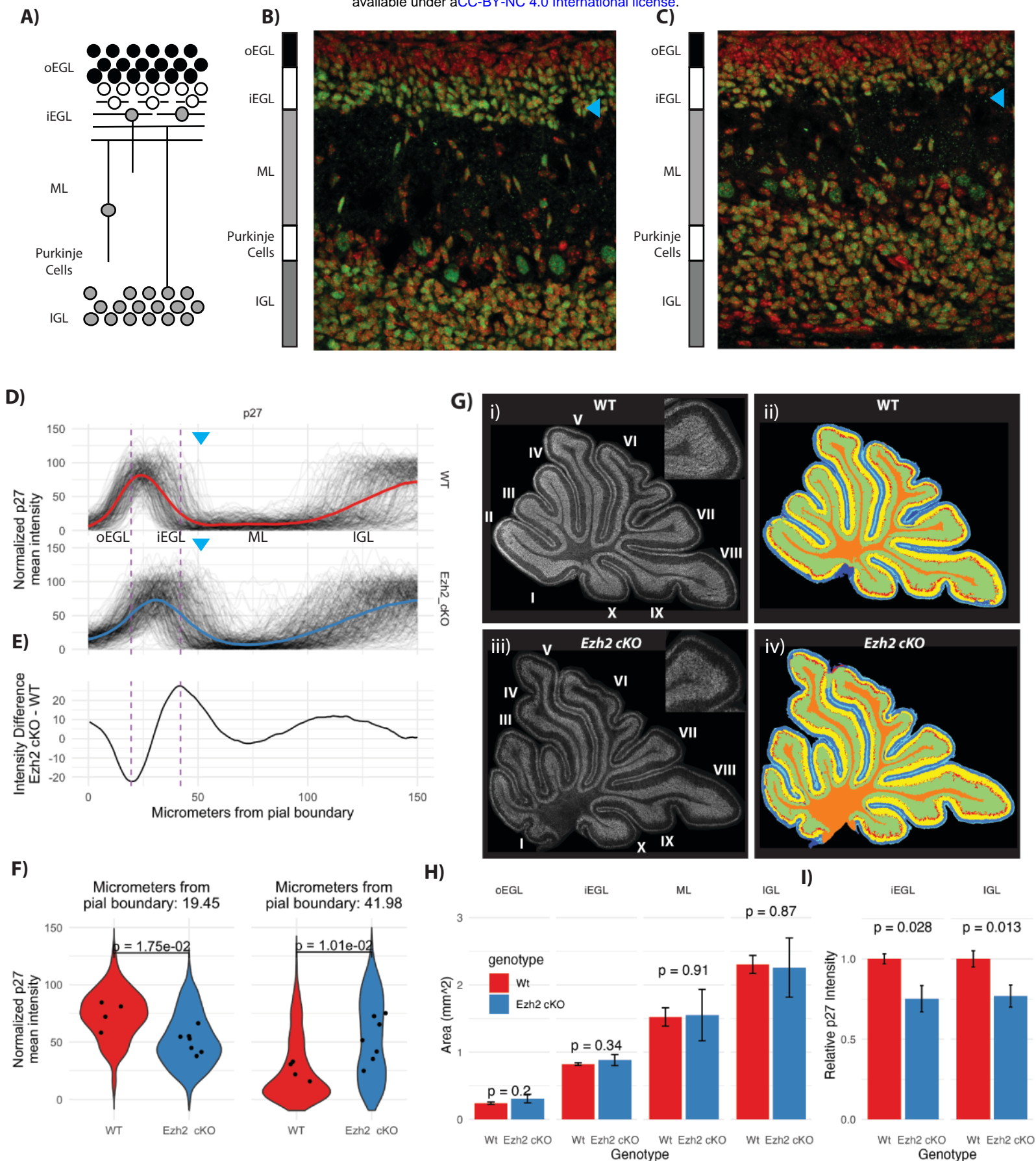
Figure 3: *Ezh2* cKO leads to a depletion of the inner EGL

A) Schematic of granule neuron (GN) development in a P7 cerebellum sagittal slice. Inner external grandule layer (iEGL), outer external granule layer (oEGL); molecular layer (ML), internal granule layer (IGL). **B)** WT and **C)** *Ezh2* cKO 40x confocal micrographs of the deep sulcus between lobule V and VI in the control and in the cKO, showing DAPI (red) and p27 (green; a cell cycle arrest marker in GNPs). In the mutant, the boundary between the inner EGL and the ML and the ML with the IGL is ill-defined. The cyan arrow indicates the position of the inner EGL, there are fewer p27 labeled cells sitting within the EGL. The cellular density is reduced in both the inner EGL and IGL. **D)** Quantification of the boundaries adjacent to the ML in WT and *Ezh2* cKO by collapsing 2D images into 1D line segments**.** The line segments for anti-p27 immunofluorescence span from the pial boundary to the IGL and show a hump of high average fluorescence at the inner EGL and the IGL. In the *Ezh2* cKO the iEGL p27 signal extends further into the ML then in the WT. The blue arrows show the approximate position of the transition between the iEGL and the ML. E) The average fluorescence intensity difference between mutant (n = 7) and WT (n = 4) shows where along the line segment from the pia to the IGL is the *Ezh2* cKO most different from the WT. Positive values are associated with p27 value being higher in the *Ezh2* cKO and is highest at the boundary of the inner EGL and the ML and to a lesser extent at the boundary between the ML and IGL. The WT shows higher signal within the inner EGL itself where the values of E are negative. **F)** Quantification of each line segment at the point where the differences between *Ezh2* cKO and WT are largest as indicated by the hashed lines seen in panel D and E. The left panel shows quantification at position where the WT had had more P27 staining then to the *Ezh2* cKO and the right panel shows the opposite.

The distribution of the values at the 2 positions in right and left panel for the 266 WT and 315 *Ezh2* cKO line segments was shown as a violin plot (a histogram that is mirrored). The dots correspond to individual mice, with multiple slides analyzed for each mouse. P-values are calculated using a T-test showing a significant increase of P27 labeling within the boundary of the EGL and ML. G) Segmentation into inner and outer EGL, ML, IGL and deep white matter using panoramic images of the entire cerebellum, labeled with DAPI, P27, NeuN. Anti-p27 over the entire P7 cerebellar section, for WT i) and *Ezh2* cKO ii). **H)** Quantification of the area for each layer in WT and *Ezh2* cKO shows no significant difference, indicating the overall structure of the cerebellum is not dramatically altered and the phenotype is limited to the early migration out of the inner EGL. **I)** Quantification of the anti-p27 fluorescence intensity by layer shows a decrease in the fluorescence in *Ezh2* cKO versus WT, for the inner EGL (p-value 0.028, t-test) and IGL (p-value 0.013, t-test). The decrease in p27 abundance suggests that the total number of neurons within the inner EGL and the IGL density of cells within those areas is reduced.
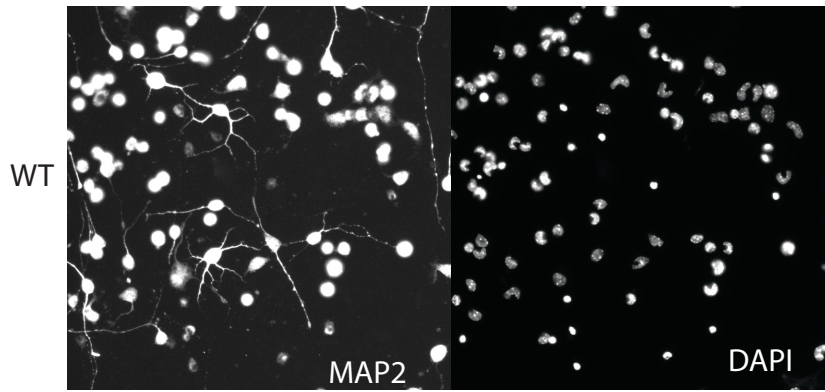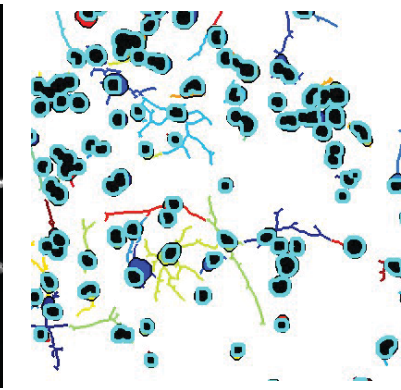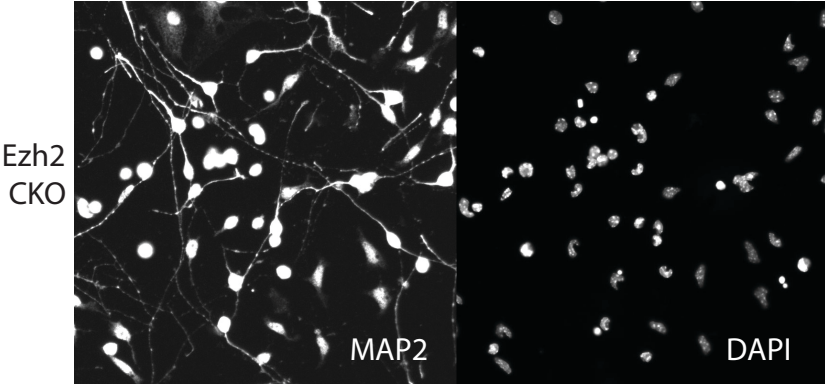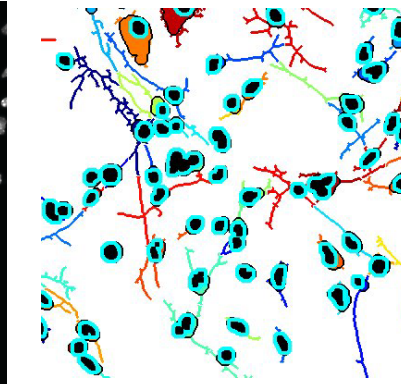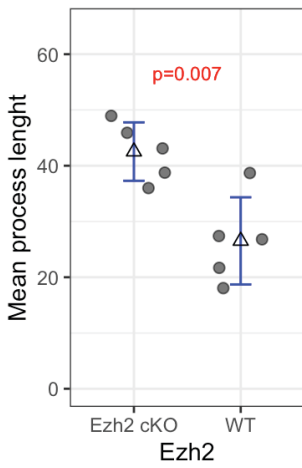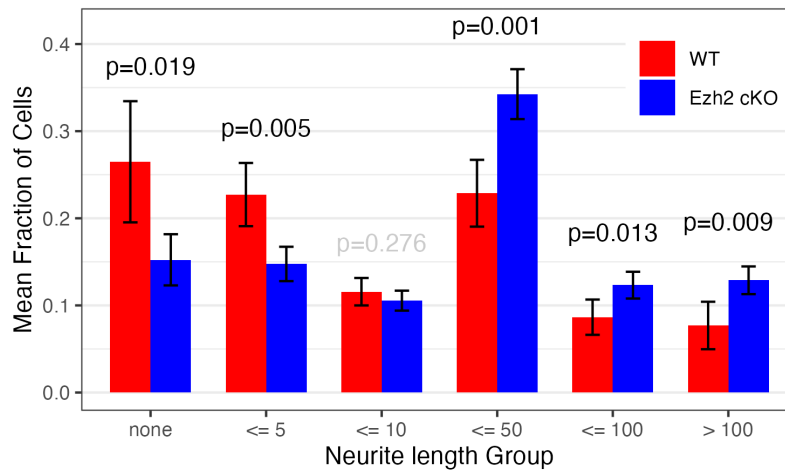
Figure 4

Figure 4: *Ezh2* **cKO leads to premature process extension and NeuN expression**.

GNPs cultured for 24 in Shh, were labeled with DAPI (nucleus) and for MAP2 (neuronal processes) (**A,C**), then segmented with Neuronctyo 2 (**B,D**). Segmented images showed increased process extension in *Ezh2* cKO (**D** for cKO versus WT in **B**). **F**) Mean process length comparison between *Ezh2* cKO and WT shows cells in *Ezh2* cKO mice had significantly longer processes (n = 5). **E**) Quantification of the number of cells with no process, a process less than 5, 10, 50, 100 pixels, or greater then 100 pixels, showed a significant increase in the number of processes longer then 50 pixels. P-value determined by T-test.
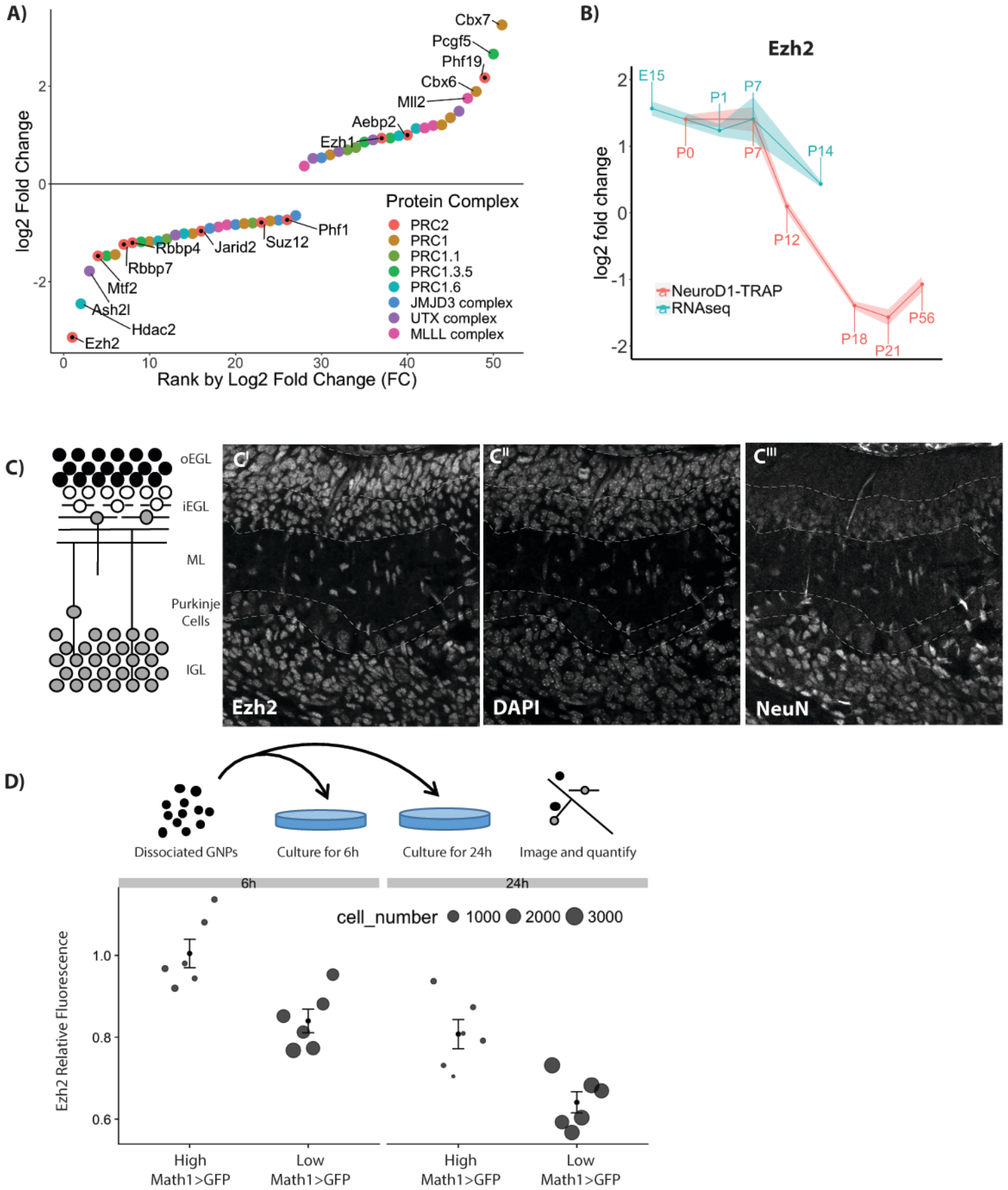
Figure 5

Figure 5: **Transcriptional regulation of known H3K27me3 effector protein complexes during granule neuron (GN) development.**

A) Rank order plot of genes that change expression during GN development shows *Ezh2* as the gene with the largest decrease in RNA abundance. The y-axis indicates the combined fold change for both datasets. **B)** RNA abundance over time for *Ezh2*. **C**) Schematic of granule neuron (GN) development in a P7 cerebellum sagittal slice. A P7 cerebellar slice stained with Anti-Ezh2 (left), DAPI (middle), and NeuN (right) shows reduced Ezh2 staining intensity in the postmitotic cells of the iEGL and EGL. **D)** Schematic of GNP culture without Shh, which causes GNPs to immediately exit cell cycle. Ezh2 protein abundance was measured after 6 h and 24, splitting cells into proliferating (high Math1>GFP) cells and non-proliferating (low Math1>GFP) cells (n=6). The decrease in Ezh2 shortly after cell cycle suggests that the decrease in Ezh2 is linked to cell cycle exit but does not show a causal relationship.
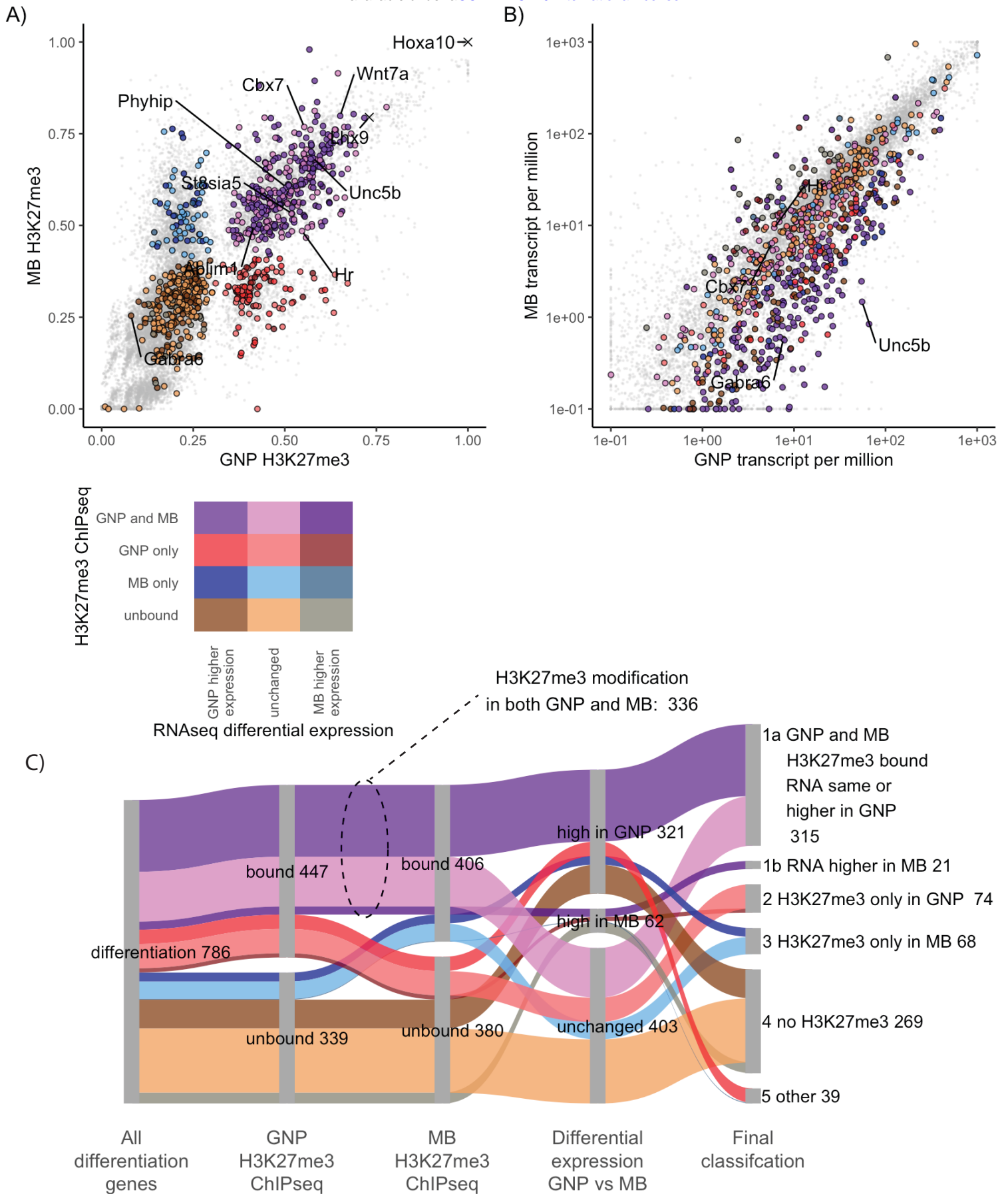
Figure 6: **In medulloblastoma cells GNP differentiation genes are transcriptionally repressed and H3K27me3 modified.**

A) H3K27me3 quantified over the promoters of GNP differentiation genes in GNPs (x-axis) and MB (y-axis). Genes are color-coded based upon H3K27me3-marked versus not marked in GNP and MB. Genes whose promoters show more H3K27me3 modification in GNP are shown in red, while those higher in MB are blue and those modified in both are purple. Duller colors (dark tones) were used if higher relative expression in MB than in GNPs. Higher saturation colors indicate gene expressed relatively higher in GNPs than in MB. The colour legend is seen bellow panel A. **B)** Transcript levels of differentiation genes in P7 GNPs, x-axis) versus in $Ptch1^{+/-}$ derived MB cells (y-axis). Colors are inherited from panel A with dark tones used for genes in MB (2 fold higher expression and adjusted p-value <0.05) and high saturation colours when higher expression in GNPs. **C)** Sankey diagram showing how the H3K27me3 modified differentiation genes are expressed in MB. The second column shows the differentiation genes in GNP separated by H3K27me3 modification. The third column compares MB H3K27me3 ChIP, showing of 447 H3K27me3 modified GNP differentiation genes, 336 (75%) of those genes are also H3K27me3 modified in MB. The fourth column shows differential expression between P7 GNPs and MB. Even when the H3K27me3 is not present in MB cells only 8% of the differentiation genes show an increase in expression in MB compared to P7 GNPs. The fifth column shows the final classification**.**
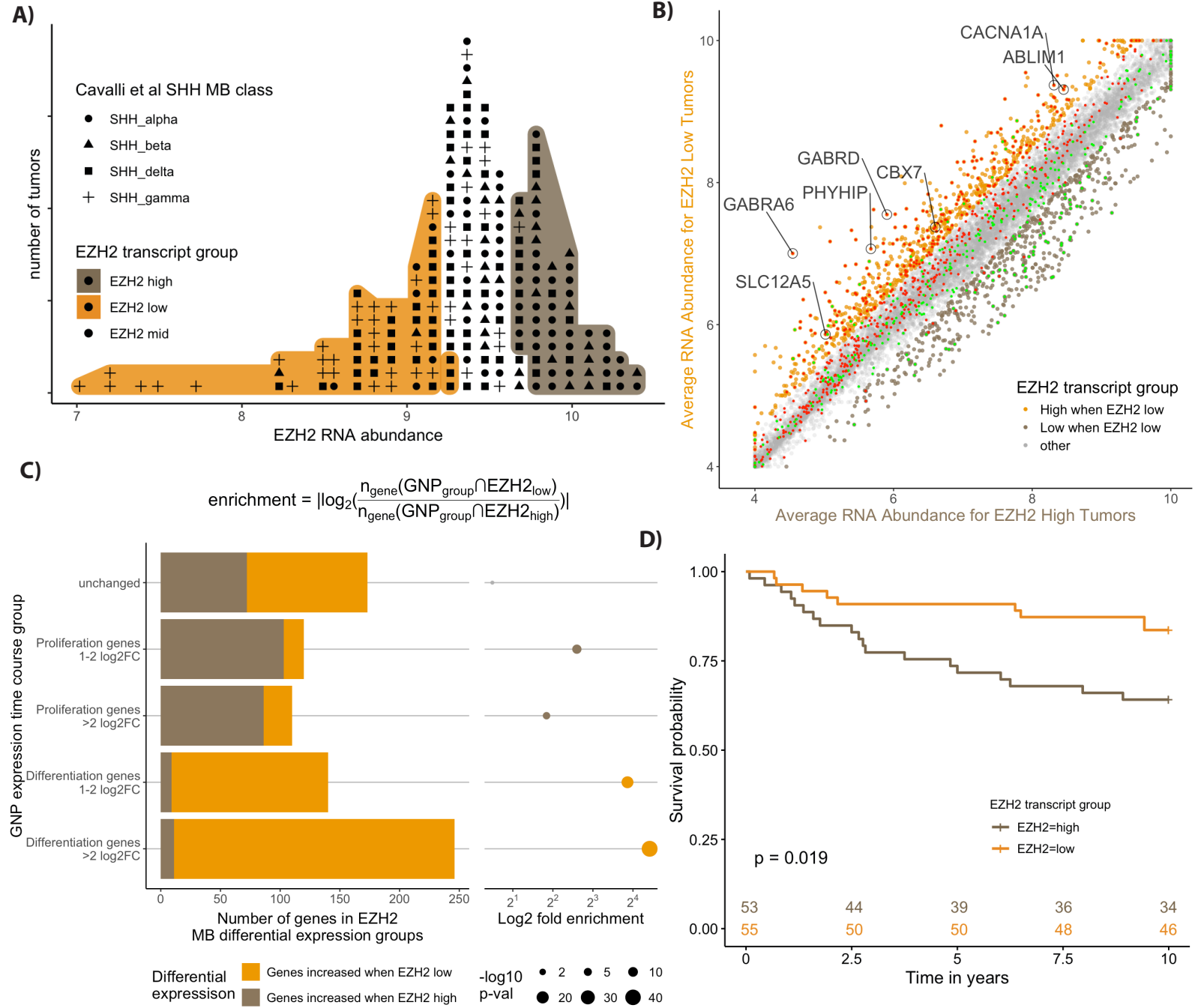
Figure 7

Figure 7: Human SHH MBs with High EZH2 are associated with worse outcome and show lower expression of GNP differentiation genes.

A) Labeled dot histogram of *EZH2* transcript abundance from 223 human SHH MB with the top (orange) and bottom (brown) 30% labeled. Each human tumor is represented as a dot with the symbols reflecting the most recent SHH MB classification (*9*). Note the high number of patients with gamma-class SHH MB with low EZH2 expression. These patients are infants with a typically good prognosis. **B)** Comparison of average gene expression between the human MB samples from the 30% highest (x-axis) and lowest EZH2 (y-axis) expressing tumours. The color labels show more highly expressed genes that are 1.5 fold higher (adjusted p < 0.05) in tumours that were low in EZH2 were labelled orange, while those that are higher in *EZH2* high tumours are brown. The GNP differentiation genes (red) show considerable overlap with the genes highest in EZH2 low tumours (orange), while the GNP proliferation genes (green) show overlap with the genes that are highest in EZH2 high tumours (brown). **C)** Quantification of the extensive overlap between GNP differentiation genes and genes highly expressed in EZH2 low human MB tumours. The categories of genes based on the GNP time course (y-axis) are quantified using a bar graph that shows the intersection of genes for each GNP group to either genes that are highly expressed when Ezh2 is low (EZH2$_{low}$) or genes that are highly expressed when Ezh2 is high (EZH2$_{high}$). Enrichment is calculated as the number of GNP group genes that intersect ($\cap$) with EZH2$_{low}$ genes over the number that intersect with EZH2$_{high}$ genes as described in the equation. The p-value is determined by the hypergeometric test.   **D)** Kaplan-Meyer curves show a significant 10 year survival difference for SHH MB patients with high versus low EZH2 transcript.
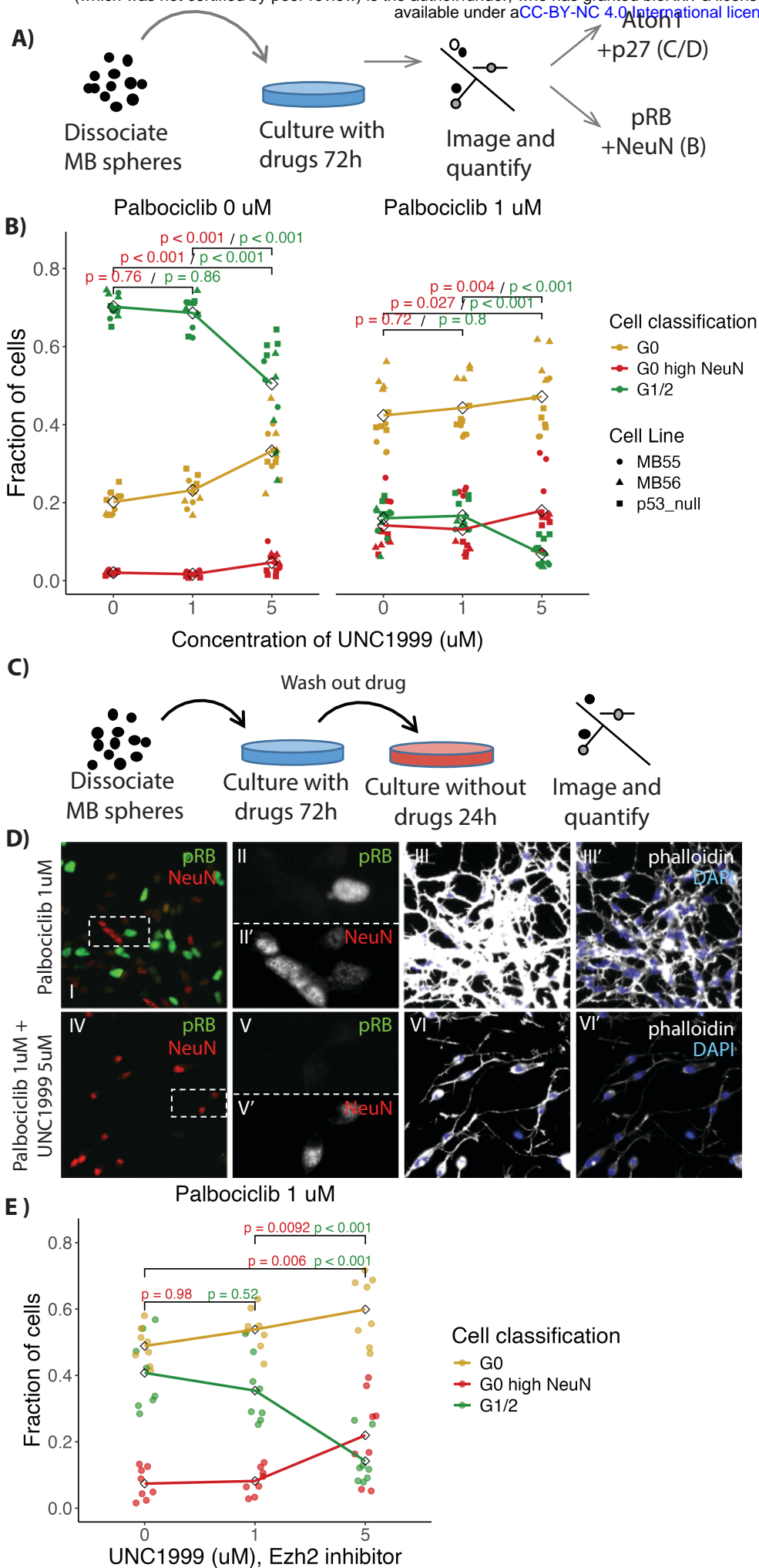
Figure 8

Figure 8: Treatment of MB cells with Ezh2 and CDK4/6 inhibitors leads to differentiation.

A) Schematic of treatment and imaging protocol. MB cells were treated using the Ezh2 inhibitor UNC1999 with or without the CDK4/6 inhibitor palbociclib. **B)** Quantification of immunofluorescence in treated MB cells (n = 16), derived from *Ptch1*$^{+/-}$ mice, stained for NeuN, pRb (Ser807/811) and DAPI to categorize the cells as in G1/2 (green), G0 (yellow) and differentiating (G0 with high NeuN (red)). Note an increase in fraction of cells scored as differentiating with combined Palbociclib and UNC1999 treatment. **C)** Schematic of treatments with inhibitors followed by drug wash out. **D)** Immunofluorescence images of fields of MB cells stained for NeuN (red), pRb (green), DAPI (blue) and phalloidin (grey) after treatment for 72h with 1 uM Palbociclib (i-iii) combined with 1 uM Palbociclib or 5 uM UNC1999 (iv-vi) followed by washout as per C. Dashed boxes in i and iv show regions enlarged in ii and v respectively, with the individual colour channels shown in separate panes. Note fewer pRB positive cells with UNC1999 and Palbociclib (iv) than with Palbociclib alone (i).   **E)** Quantification of fractions of cells in G0, G1/2, and G0 and differentiating as described in B (n = 8). Note that the MB cells treated with both UNC1999 and Palbociclib showed persistent cell cycle exit even after washout. P-values in B and E calculated using ANOVA with post-hoc Tukey test.